

A New Fiber Mirror Production Setup

Michael Kubista

Masterarbeit in Physik
angefertigt im Institut für Angewandte Physik

vorgelegt der
Mathematisch-Naturwissenschaftlichen Fakultät
der
Rheinischen Friedrich-Wilhelms-Universität
Bonn

Oktober 2017

I hereby declare that this thesis was formulated by myself and that no sources or tools other than those cited were used.

Bonn,
Date

.....
Signature

1. Gutachter: Prof. Dr. Dieter Meschede
2. Gutachter: Prof. Dr. Stefan Linden

Contents

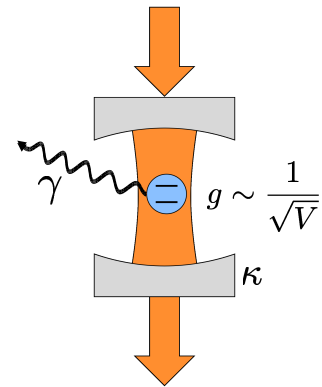
1	Introduction	1
2	Theoretical Background	3
2.1	Optical Resonators	3
2.1.1	Fabry-Perot Resonators	3
2.1.2	Gaussian Beams	5
2.1.3	Fiber Fabry-Perot Cavities	7
2.1.4	Optical Fibers	8
2.2	Ablation Process	9
3	Fiber Mirror Production	13
3.1	Experimental Setup	13
3.1.1	CO ₂ Laser	14
3.1.2	Optical Setup	17
3.1.3	Beam Profiling	18
3.2	Production Process	20
3.2.1	Fiber Preparation	20
3.2.2	Positioning	21
3.2.3	Ablation Sequence	22
3.2.4	Control	23
4	Surface Profiling	27
4.1	White Light Interferometry	27
4.2	Mirau Interferometer	28
4.2.1	Mirau Objective	28
4.2.2	Illumination	30
4.3	Analysis Methods	30
4.3.1	Brightest Pixel Method	31
4.3.2	Fourier Analysis	33
4.3.3	Phase Unwrapping	34
4.4	Radius of Curvature Extraction	35
4.5	Comparison	37
5	Results	39
5.1	Radius of Curvature	39
5.2	Eccentricity	39
6	Summary and Outlook	41
6.1	Summary	41

6.2	Technical Improvements	41
6.3	Advanced Techniques	42
6.3.1	Dot-Milling Technique	42
6.3.2	GRIN Lenses	42
	Bibliography	45
	A Knife Edge Method	51
	List of Figures	53

Introduction

In 1946, Purcell suggested that placing an atom inside an optical resonator could enhance spontaneous emission [1], laying the foundation for the field of cavity quantum electrodynamics [2]. One of the most important figures of merit to characterize the enhanced light-atom interaction in a cavity is the cooperativity $C = g^2/2\kappa\gamma$, where g is the coupling strength between atom and cavity, κ is the decay rate of the intracavity field and γ is the excited state decay rate. Strong coupling ($g \gg (\gamma, \kappa)$) between atoms and light inside such a cavity has numerous interesting applications. It can be an important tool in quantum information processing [3], and provides a method to investigate more fundamental concepts such as entanglement and decoherence [4, 5]. The atom-light interaction in these systems can be utilized to create quantum memories, where the information encoded in a flying qubit, here a photon, is transferred to the internal states of a stationary qubit, here an atom (or atoms) [6].

The coupling strength is related to the mode volume of the cavity by $g \sim \mathbf{d} \cdot \mathbf{E} \sim V^{-1/2}$, where the mode volume is $V = (\pi/4) \cdot w_0 \cdot L_{\text{cav}}$ with waist size w_0 and cavity length L_{cav} . Hence, the cooperativity can be increased by decreasing the mode volume, i.e. by building smaller cavities. This is of particular interest for application which need a high bandwidth κ and the strong coupling regime at the same time. To decrease the mode volume, the radii of curvature of the mirrors must be as small as possible. Conventional mirror polishing techniques cannot produce arbitrarily small radii of curvature, posing a technical limit for the use of bulk cavities. In addition, the size of these mirrors also restricts optical access to the cavity. Both of these limits can be overcome by fiber-based resonators [7, 8]. In 2006, Steinmetz et.al. reported on a technique to directly attach mirrors to fiber end facets [9]. This was done in a two step process: First, a mirror is coated onto a convex substrate, then a fiber is glued on top and lifted off the substrate with the mirror attached. Later, CO₂ lasers came into use to micro-fabricate concave mirrors directly onto the fiber end facets by ablation and subsequent coating [10]. Treating silica with powerful CO₂ lasers had previously been used to create micro lenses [11], to polish glass surfaces [12] or to repair laser induced damage [13]. Even though in these cases evaporation had mostly been an unwanted effect, the insight gained by studying the responsible mechanisms in these contexts became useful when starting to fabricate concave micro-structures. Since there is a strong correlation between depth and radius of curvature of the resulting depression [14, 15], the size of Fiber Fabry-Perot cavities manufactured this way also has a natural stability limit. With decreasing radius of curvature the depth increases such that the stability criterion for a plano-concave resonator $L < R$ ($L < 2R$ for biconcave) does not allow for cavities with radii of



curvature below $5\ \mu\text{m}$ ($10\ \mu\text{m}$). Here, further processing techniques must be employed to achieve even shorter cavities [15]. Newer developments include the use of GRIN lenses to improve mode matching [16] and dot milling to create larger spherical structures using a series of pulses [17].

The purpose of my thesis project is to set up a new, improved fiber mirror production facility. While our group already had a laser ablation setup, this system was optimized to produce mirrors with sizes needed specifically for our experiments, i.e. with a radii of curvature of $\sim 170\ \mu\text{m}$ [18]. One of the goals of the new setup is a higher versatility, which includes the capability to produce mirrors with a wide range of radii of curvature. This is necessary as neutral atom-light coupling is not the only application of fiber cavities, and the requirements on the mirror sizes can vary greatly between them. Experiments with single ions are performed in cavities with mirror radii of curvature in the range from about $200\ \mu\text{m}$ - $560\ \mu\text{m}$ [19, 20]. Much smaller cavities are employed when coupling to solid state emitters such as quantum dots or NV-centers. Here, examples for radii of curvature are $42\ \mu\text{m}$ [21] and $18.4\ \mu\text{m}$ [22] respectively. Other applications of fiber cavities, going beyond the coupling to atoms or quasi-atoms, include opto-mechanical devices [23], spectral filters for use in computer networks [24], and scanning fiber microscopes to image nanosystems [25].

A further important goal is to improve the production quality. This will be achieved by using state of the art elements in our setup. These include a new laser with a wavelength of $9.3\ \mu\text{m}$ ¹ for a better control of the ablation process due to higher absorption [26], a phase shifting mirror to create a circularly polarized beam [27], and high precision translation stages² for more precise and reproducible fiber positioning. In addition we will be using a new fiber cleaver³ to reduce mirror decentration.

Finally, I will present the results of the first ablation craters produced with the new setup.

¹Coherent Diamond C-55L 9.3

²Aerotech ANT95-L Nanopositioning Stages

³Nyfors AutoCleaver™

Theoretical Background

To discuss the production of mirrors for fiber cavities, it is useful to give some theoretical background on optical resonators and their modes, on optical fibers and fiber based resonators, and on the ablation process itself.

2.1 Optical Resonators

Optical resonators, which efficiently confine and store light, can be employed to enhance the interaction probability between light and matter. This chapter summarizes the main properties of the type of resonator used in our Fiber Cavity Quantum Electrodynamics (FCQED) experiments, the Fabry-Perot resonator.

2.1.1 Fabry-Perot Resonators

In its most simple form, a Fabry-Perot resonator consists of a pair of highly reflective mirrors facing each other. Between them, injected light fields circulate by being reflected back and forth, and can interfere constructively if meeting certain resonance conditions. These so-called longitudinal modes supported by the resonator can be pictured either as standing waves¹ (figure 2.1 a)) or as self reproducing traveling waves (figure 2.1 b)). In the latter case, the phase shift picked up at each round trip is

$$\varphi = 2kd = \frac{4\pi\nu d}{c}, \quad (2.1)$$

where φ must be a multiple of 2π and d is the mirror spacing, i.e. the cavity length d must be an integer multiple of $\lambda/2$. This condition is fulfilled by an infinite number of equally spaced frequencies with

$$\nu_q = \frac{q \cdot 2d}{c} = q \cdot \Delta_{\text{FSR}}, \quad (2.2)$$

where q is an integer and Δ_{FSR} is the so-called free spectral range. This description assumes an ideal, lossless resonator. Taking into account the losses given by absorption, scattering and finite reflectivities of the mirrors, one can introduce the round trip intensity attenuation factor $r^2 = R_1 R_2 \exp(-2\alpha_s d)$, where $\mathcal{R}_{1,2} = r_{1,2}^2$ are the mirror reflectances and α_s denotes losses. The spectral response can then be expressed

¹This only applies to the two-mirror configuration introduced here. Other types such as the bow-tie resonator do not have standing waves.

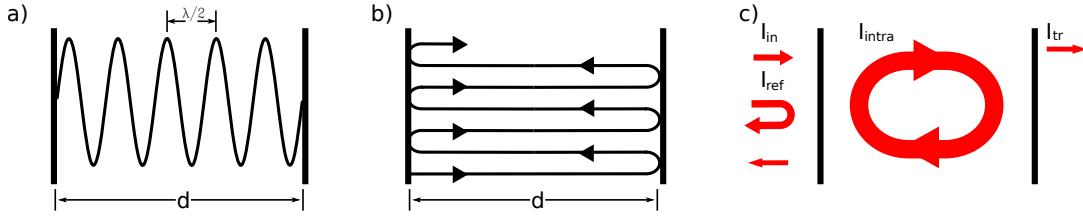


Figure 2.1: a) Intensity of a resonator mode as standing wave. b) Intracavity field as self-reproducing travelling wave. c) Incoming, reflected, transmitted and intracavity intensities of a lossy resonator.

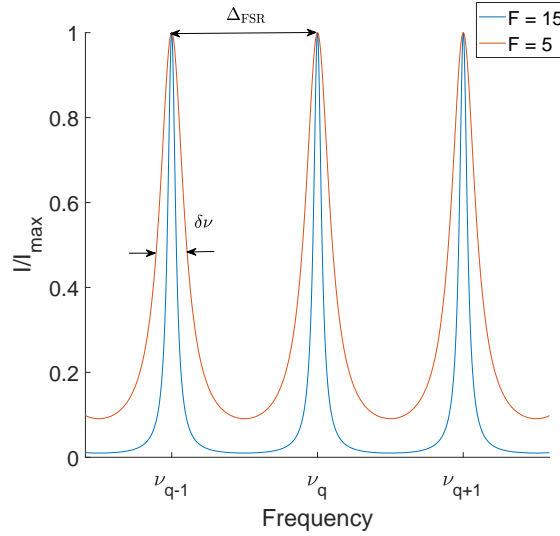


Figure 2.2: Normalized intensity as a function of frequency inside a lossy resonator for different values of the finesse.

as [28]

$$I_{res} = \frac{I_{max}}{1 + (2\mathcal{F}/\pi)^2 \sin^2(\pi\nu/\Delta_{FSR})}, \quad \text{with} \quad I_{max} = \frac{I_0}{(1-r)^2}. \quad (2.3)$$

The parameter \mathcal{F} in eq. 2.3 is called the finesse of the resonator and is defined as

$$\mathcal{F} = \frac{\pi\sqrt{r}}{1-r} \quad (2.4)$$

As a result, the spectral response of a lossy cavity consists of a collection of resonances with finite line widths (see figure 2.2). The full width half maximum $\delta\nu$ of these peaks can be expressed in terms of the finesse as

$$\delta\nu = \frac{\Delta_{FSR}}{\mathcal{F}}. \quad (2.5)$$

This relationship provides an experimental way to determine resonator losses.

For light to be able to couple into a cavity, the spacial mode of the incoming beam must match the transversal cavity mode. This means, wave front curvature and mode field diameter of the incoming beam must match at the position of the incoupling mirror (see figure 2.3). The part $(1 - \epsilon)P_{in}$, where ϵ is

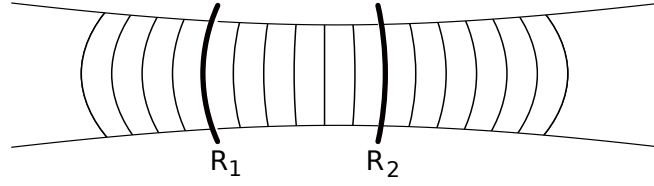


Figure 2.3: Mode matched cavity with $R_1 \neq R_2$: The phase front and the diameter of the cavity mode and the free-space beam are the same at the mirror positions

the mode matching efficiency, is reflected (see figure 2.2 c)). How much of the mode-matched light is entering the cavity is determined by the impedance-matching efficiency η_{imp} with

$$\eta_{\text{imp}} = \left(1 - \left(\frac{\mathcal{T}_1 - \mathcal{T}_2 + 2\mathcal{L}}{\mathcal{T}_1 + \mathcal{T}_2 + 2\mathcal{L}} \right)^2 \right), \quad (2.6)$$

where \mathcal{T}_1 is the transmission of the input mirror, \mathcal{T}_2 is the transmission of the second mirror, and $2\mathcal{L}$ are the resonator losses. For conventional cavities, the mode matching condition can be fulfilled by shaping the incoming beam with appropriate optics.

So far, we have ignored the stability criteria of these resonators. Misalignment of the cavity mirrors as well as diffraction effects can cause light to escape the resonator. Ray confinement can be improved by using spherical mirrors. Here also only certain configurations provide a stable cavity. Defining the g parameters $g_{1,2} = 1 + d/R_{1,2}$, where $R_{1,2}$ are the radii of curvature², the confinement condition for stable resonators takes the form

$$0 \leq g_1 g_2 \leq 1. \quad (2.7)$$

Several special cases of mirror configurations can be seen in figure 2.4. These criteria are the reason, that even fiber cavities cannot be made arbitrarily short when the mirror is fabricated via laser ablation. In this procedure, a smaller radius of curvature coincides with a higher structure depth (see section 2.2), prohibiting stable configurations for biconcave cavities with radii of curvature below $\lesssim 10 \mu\text{m}$ [15]. The fundamental mode of the spacial distribution of light inside Fabry-Perot cavities with spherical mirrors is given by Gaussian beams, which are further described in the next section.

2.1.2 Gaussian Beams

Gaussian beams are solutions of the paraxial Helmholtz equation

$$\left(\frac{\partial^2}{\partial x^2} + \frac{\partial^2}{\partial y^2} - 2ik \frac{\partial}{\partial z} \right) E = 0 \quad (2.8)$$

and describe both the resonator modes of optical cavities with spherical mirrors as well as propagating laser beams. The electric field of its TEM_{00} fundamental mode traveling in the z -direction is given at a point in time by:

$$E(r, z) = E_0 \frac{w_0}{w(z)} \exp\left(\frac{-r^2}{w(z)^2}\right) \exp\left(-i\left(kz + k\frac{r^2}{2R(z)} - \psi(z)\right)\right), \quad (2.9)$$

²Using the definition $R < 0$ for concave and $R > 0$ for convex mirrors

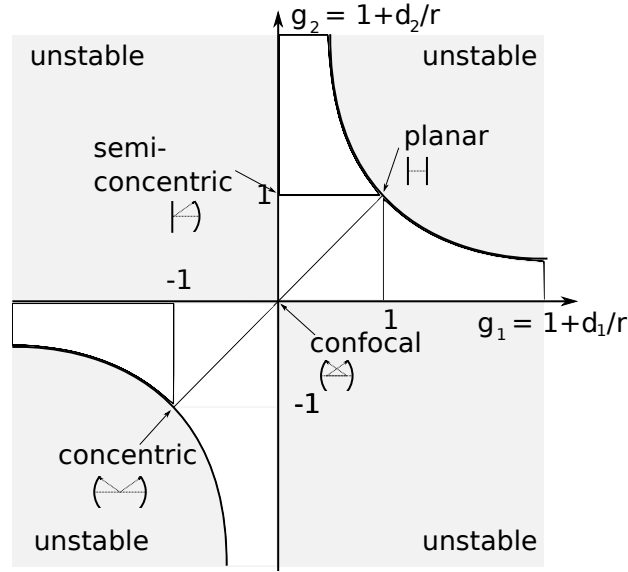


Figure 2.4: Stability of optical resonators. In the white area the stability criterion $0 \leq g_1 g_2 \leq 1$ is fulfilled.

where $r^2 = x^2 + y^2$ and with the following beam parameters:

$$\text{Beam Width} \quad w(z) = w_0 \sqrt{1 + \left(\frac{z}{z_0}\right)^2} \quad (2.10a)$$

$$\text{Wavefront Radius of Curvature} \quad R(z) = z \left[1 + \left(\frac{z_0}{z}\right)^2 \right] \quad (2.10b)$$

$$\text{Beam Waist} \quad w_0 = \left(\frac{\lambda z_0}{\pi}\right)^{1/2} \quad (2.10c)$$

$$\text{Gouy Phase} \quad \psi(z) = \arctan\left(\frac{z}{z_0}\right) \quad (2.10d)$$

$$\text{Beam Divergence} \quad \theta_{\text{div}} \approx \frac{\lambda}{\pi w_0} \quad (2.10e)$$

The parameter z_0 is the so-called Rayleigh-length, i.e. the distance from the waist at which the beam width has increased by a factor of $\sqrt{2}$.

In the paraxial approximation the resonance frequencies of the fundamental mode are independent of the mirror radii R . Corrections to this paraxial model show that for a plano-convex cavity there is a frequency splitting between the polarization eigenmodes of

$$\Delta\nu = \frac{\Delta_{FSR}}{2\pi k} \frac{R_1 - R_2}{R_1 R_2}, \quad (2.11)$$

where R_1 and R_2 are the radii of curvature along the major and minor axes of an ellipsoid fitted to the central region of the mirror [27]. This means that the produced fiber mirrors need to be as circular as possible. In addition to the fundamental mode, there are higher order Hermite-Gaussian, or TEM_{nm} modes, with more complicated intensity distributions, which are also solutions of the paraxial Helmholtz

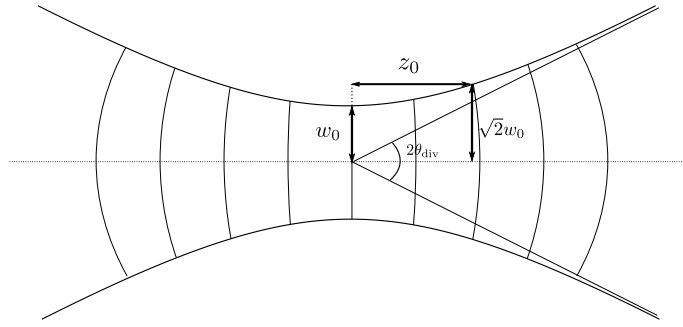


Figure 2.5: Gaussian beam with wave fronts, waist w_0 , Rayleigh length z_0 , and divergence angle θ_{div}

equation 2.8. They add additional resonator modes for cavity lengths of

$$L_{qnm} = \left(q + \frac{n + m + 1}{\pi} \cos^{-1} \sqrt{g} \right) \frac{\lambda}{2}, \quad (2.12)$$

where for a plano-concave cavity $g = 1 - L_{qnm}/R_{\text{eff}}$. This provides a way to experimentally determine the effective mirror radius R_{eff} [15].

For propagating beams the presence of higher order modes increases the divergence angle θ_{div} . The deviation from a perfectly Gaussian beam is then quantified by the beam quality factor

$$M^2 = \frac{\pi}{\lambda} w_o \theta_{\text{div}}, \quad (2.13)$$

where for a perfect Gaussian TEM_{00} beam $M^2 = 1$.

2.1.3 Fiber Fabry-Perot Cavities



Property	Polished mirrors [29]	Fiber Cavity [30]
Length l_0	158.5 μm	93.4 μm
Mode waist w_0	23 μm	4.4 μm
Mode volume V_{mode}	70 000 μm^3	1 400 μm^3
Coupling strength g_0	18 MHz $\cdot 2\pi$	120 MHz $\cdot 2\pi$
Finesse \mathcal{F}	1 000 000	30 000
Cavity field decay κ	0.6 MHz $\cdot 2\pi$	25 MHz $\cdot 2\pi$
Cooperativity C_{max}	≈ 100	≈ 100

Figure 2.6: Comparison of size and properties between the two cavity types used in our group.

One way to build Fabry-Perot cavities with a very low mode volume is using high reflectivity coated end facets of optical fibers (further discussed in section 2.1.4) as resonator mirrors. They can reduce the

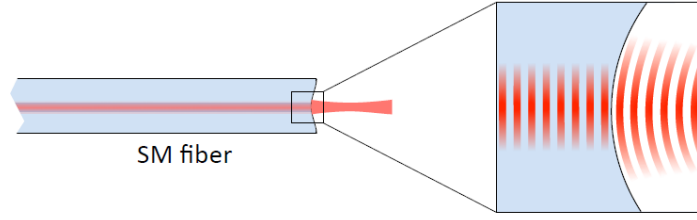


Figure 2.7: Mode mismatch between fiber mode and cavity mode

mode volume by orders of magnitude, compared to macroscopic cavities with polished mirrors. Figure 2.6 shows a comparison between a macroscopic and a fiber-based cavity, both employed in the CQED experiments performed in our group. Using fiber end facets as mirror substrates gives rise to several additional advantages: The whole resonator is much smaller than traditional cavities, leading to better scalability. It also allows for better optical access. In fiber cavities it is much easier to image atoms inside the cavity using high numerical aperture lenses perpendicular to the cavity axis than it is in macroscopic cavities. Finally, the cavity mode is intrinsically fiber-coupled, which is desirable for its implementation in fiber-based networks. This last advantage, however, also comes at a cost. Single mode optical fibers leave no room for mode matching optics, severely limiting the coupling efficiency and prohibiting any mode matching adjustments once the cavity has been built. The mode of the incoming field is purely defined by the fiber: As depicted in figure 2.7, the wave front in a single mode fiber is flat and the mode field diameter (MFD) is determined by the size of the fiber core and the wavelength of the guided light. On the other hand, the wave front of the intracavity field at the position of the mirror is curved with the same radius at curvature as the mirror, and the spot size is usually larger than the MFD of the fiber.

2.1.4 Optical Fibers

Optical fibers are flexible, cylindrical, dielectric waveguides made from Germanium doped fused silica. Due to their low absorption in the near infrared regime they are suitable candidates for long distance transmission of photons as needed for quantum communication. Their ability to guide light results from total internal reflection due to a difference in refractive index between the core and the cladding (see figure 2.8), usually realized by doping the silica with elements such as germanium, boron, or titanium. The transmission properties are then mainly decided by size and shape of the core and the refractive index profile. The first important distinction to be made is between single mode fibers with a small core diameter, typically around or below $8 \mu\text{m}$, and multi mode fibers with a larger core. A convenient parameter to determine the number of modes guided by a step index fiber is the V-parameter

$$V = \frac{2\pi a}{\lambda_0} \sqrt{n_{co}^2 - n_{cl}^2}, \quad (2.14)$$

where a denotes the core radius and n_{co} and n_{cl} are the indices of refraction of core and cladding respectively. For $V < 2.405$ only the fundamental mode is guided, the fiber is said to be single mode. (figure 2.9 a)) For multi mode fibers (figure 2.9 b)) with $V \gg 1$ the number of guided modes behaves as

$$M \approx \frac{4}{\pi^2} V^2. \quad (2.15)$$

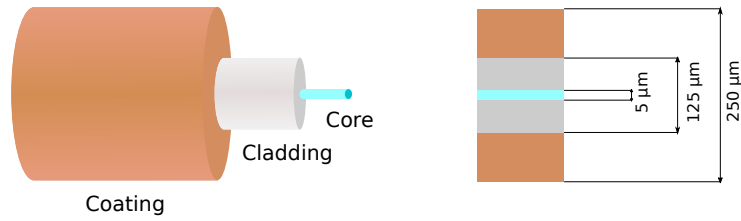


Figure 2.8: Schematic and typical dimensions of a single mode fiber

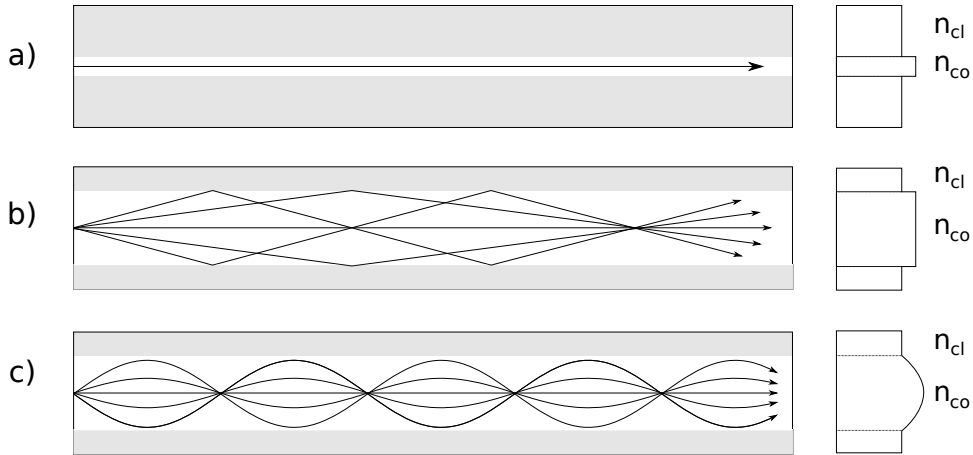


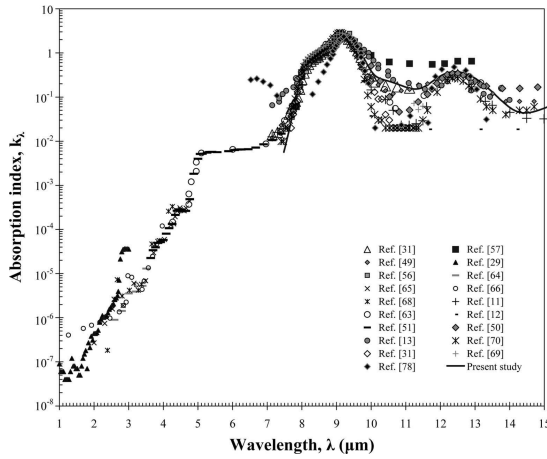
Figure 2.9: Fiber types, their refractive index profiles, and examples of their modes: a) step index single mode, b) step index multi mode, c) graded index

A detailed derivation of these relationships can be found in numerous textbooks, such as [28]. By shifting from a step index to a graded index profile one can create a fiber that self focuses the guided modes, reduces modal dispersion, and whose mode field geometry at the output is dependent on its length. (figure 2.9 c)) The usefulness of this fiber type for cavities will be further discussed in section 6.3.2.

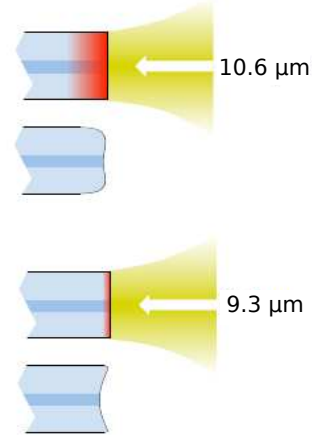
2.2 Ablation Process

Silica has an absorption peak centered around $9.3 \mu\text{m}$ resulting from an asymmetrical Si-O-Si vibrational resonance [26]. This makes CO_2 lasers with a wavelength range around $9\text{--}11 \mu\text{m}$ an ideal tool for thermal machining of quartz glass surfaces. The fabrication of micro mirrors using CO_2 laser pulses takes place in a parameter regime, where thermal evaporation leads to the formation of a concave structure. Surface melting leads to a mirror smoothness on an atomic scale. However, the molten layer should not be so thick that surface tension causes it to form convex structures or rounded edges [10]. For this purpose we will use a $9.3 \mu\text{m}$ laser, because at this wavelength the absorption length is shorter than at the more commonly used $10.6 \mu\text{m}$ (see figure 2.10). For evaporation of fused silica to occur, its temperature must rise above $T \sim 2600 \text{ K}$. At $T > 3000 \text{ K}$, the vapor pressure exceeds the ambient pressure, allowing for high evaporation rates [31]. The temperature dependent velocity of the evaporation front is then given by

$$v(\rho, t) = v_0 \exp\left[\frac{-U}{k_B T(\rho, t)}\right], \quad (2.16)$$



(a) Absorption index for fused silica in the range between 1 and 15 μm . Taken from [26]



(b) The higher absorption at 9.3 μm leads to a thinner heated layer and less rounding of the edges

Figure 2.10: Wavelength dependence of the ablation process

with the radial coordinate ρ , the latent heat $U = 3.6$ eV and $v_0 = 3.8 \times 10^5$ cm/s [13].

The majority of the laser power is absorbed at the surface, so that a beam with a Gaussian intensity profile $I(\rho, t) = I(t) \exp(-2\rho^2/w_0^2)$ results in a temperature profile

$$T(\rho, t) = \frac{2Aw_0^2}{D} \sqrt{\kappa/\pi} \int_0^t \frac{I(t-t')}{\sqrt{t(2w_0^2 + 4Dt')}} \exp\left(\frac{-\rho^2}{2w_0^2 + 4Dt'}\right) dt', \quad (2.17)$$

where A is a wavelength dependent absorption coefficient, D is the thermal diffusion constant and κ is the thermal conductivity. For a pulse of length τ and constant intensity the depth of the structure then takes the form

$$z(\rho) = z_0 \exp\left(-\frac{U}{k_B T(0, \tau)} \frac{\rho^2}{2w_0^2}\right), \quad (2.18)$$

with

$$T(0, \tau) = \frac{AP}{\sqrt{2\pi^3} w_0 \kappa} \arctan\left(\frac{2D}{w_0^0 \tau}\right). \quad (2.19)$$

Here, we see that the resulting structure will have a Gaussian shape which can in the center be approximated by a spherical depression. The latter is the desired shape for fiber mirrors.

Finally, the 1/e diameter can be estimated as [13]

$$d \approx 2w_0 \sqrt{\frac{k_B T(0, \tau)}{U}} \quad (2.20)$$

Equations 2.18 and 2.20 shows that the important ablation parameters determining the shape of the structure are laser power, beam waist, and pulse length.

This model, however, makes several approximations [32, 33]:

- **Absorption length:** In this model the laser is treated as a surface source, i.e. the finite absorption length is ignored. Since the absorption length decreases with temperature [34], this is a valid approximation, once temperatures sufficient for evaporation have been reached. Furthermore, using a laser with a wavelength of 9.3 μm instead of the more common 10.6 μm leads to a decreased absorption length even at lower temperatures.
- **Evaporation:** This model ignores the loss of latent heat by evaporated material. This energy is then no longer available to break the bonds to neighboring atoms and molecules. The corresponding heat flux density would be $\Phi_{\text{evap}} = \frac{\rho}{M} N_A v_0 U \exp(-U/k_B T)$.
- **Radiation:** This model doesn't take into account energy loss by blackbody radiation $\Phi_{\text{rad}} = \epsilon \sigma (T^4 - T_{\text{amb}}^4)$. Here, σ is the Stefan-Boltzmann constant, ϵ is the material's emissivity and T_{amb} is the ambient temperature.
- **Linear Conduction:** This model assumes the thermal conductivity to be constant, which is no longer the case in the temperature regime needed for evaporation. Here, one can use the empirical formula

$$\kappa(T) = \kappa_0 + \beta T^3 = 0.01(1 + 1.7 \cdot 10^{-9} T^3) (\text{W/cm K}) = \kappa_0 f \left(\frac{T}{T_0} \right)^3, \quad (2.21)$$
 with $\kappa_0 = 0.01 \text{ W/cm K}$ at room temperature [13].
- **Fiber geometry:** This model assumes a completely filled half space of material, i.e. it disregards the finite size of the fiber tips. On the edges convection is not available as a means for heat transport any more.
- **Contact with the fiber holder:** Thermal coupling of the fiber to its holder is neglected. Reference [32] reports that for pulse durations $> 80 \text{ ms}$ there is a strong dependence between the properties of the created structure and the length of the fiber tip protruding from the holder.

All these factors make it challenging to precisely predict the resulting structures for given ablation parameters. They have to be determined experimentally. By varying laser power, pulse length and beam waist, approximately Gaussian profiles with radii of curvature $R = 5 \dots 2000 \mu\text{m}$ and depths $D = 0.01 \dots 4 \mu\text{m}$ can be produced [14, 15].

Fiber Mirror Production

As depicted in figure 3.1, the process of constructing a fiber cavity, as reported in [10], can be divided into four steps: high precision fiber cleaving, laser ablation to produce the concave structure on the fiber end facet, high reflectivity coating to turn the structures into mirrors, and cavity assembly by aligning two fibers in such a way that they form a suitable resonator for FCQED experiments. In this chapter, I will describe our implementation of the ablation process in detail, as this is the main goal of my master project. It is also necessary to include a brief discussion of the cleaving process. The third and fourth steps of the process are beyond the scope of this thesis.

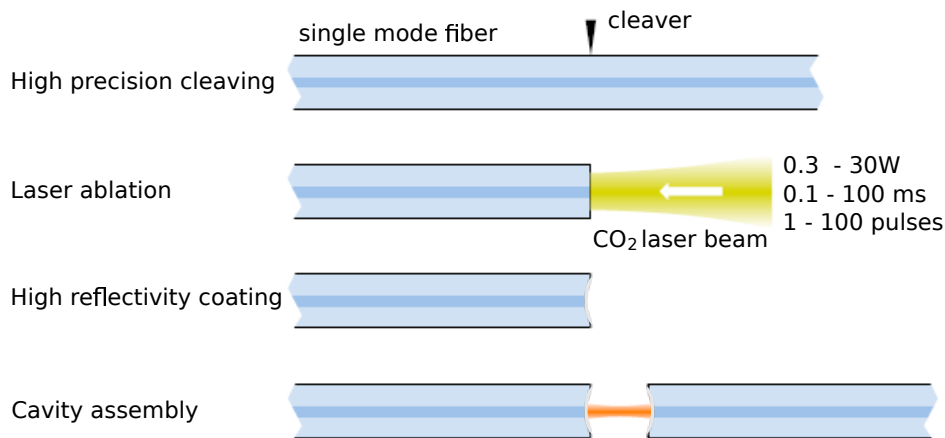


Figure 3.1: The four steps for fiber cavity construction: high precision cleaving, laser ablation, high reflectivity coating, and cavity alignment.

3.1 Experimental Setup

In order to generate laser pulses suitable for the fiber mirror production by glass ablation, as described in section 2.2, the setup must fulfill certain requirements: First, the transversal intensity profile of the laser beam must be as close to a circularly symmetric Gaussian profile as possible to create the desired structure geometry. Second, the generated pulses must be reproducible, which includes ensuring power

stability and the ability to monitor this power. Finally, we have to be able to position the fibers very precisely with respect to the laser beam waist.

3.1.1 CO₂ Laser

The ablation pulses are generated by a CO₂ laser. The latter are molecular gas lasers with relevant transitions between vibration-rotation energy levels in the infrared regime. The upper state is an antisymmetric stretching vibration (001), while the lower levels for the 10.6 μm and the 9.6 μm emission lines are a symmetric stretching vibration (100) and a bending vibration (020) respectively (see figure 3.2(a)). These levels are split into rotational sublevels, leading to bands of emission lines centered around 10.4 μm and 9.4 μm (see figure 3.2(b)). Specific laser lines can be chosen by using a grating as one of the resonator mirrors. The long lived (001) level is populated by discharge, either directly, or more efficiently by the addition of molecular nitrogen and the subsequent energy transfer from the excited nitrogen to the CO₂.

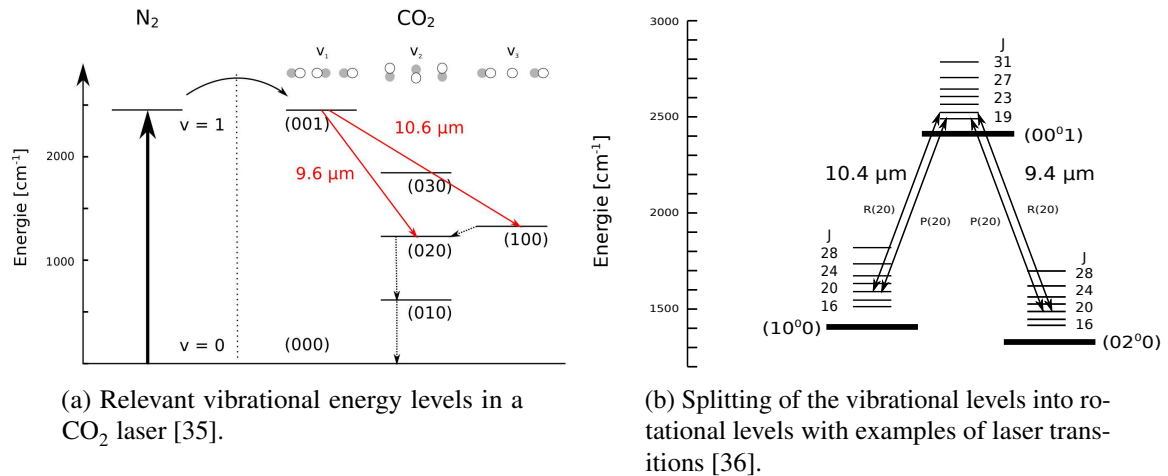


Figure 3.2: CO₂ Laser levels.

The CO₂ laser¹ used in our setup has a wave guide configuration (see figure 3.3) in which the gas mixture is excited by radio frequency (RF) electric fields. This configuration allows for higher gas

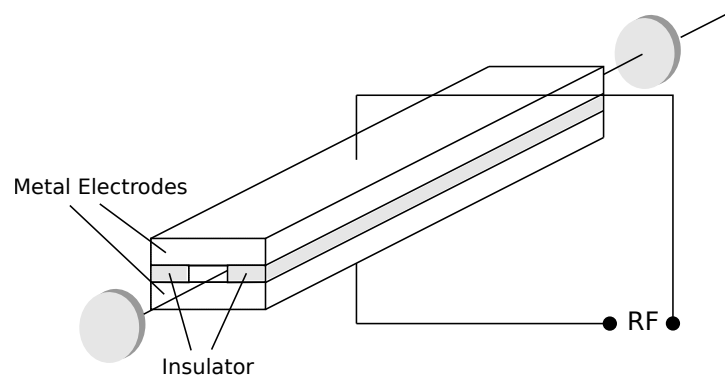


Figure 3.3: CO₂ laser in wave guide configuration [35].

¹Coherent Diamond C-55L 9.3

pressure compared to a conventional discharge tube, increasing gain and laser power per volume [36]. The laser's maximum output power is 55 W at 9.3 μm . This output power is controlled by changing the duty cycle of the pulse width modulated RF drive signal. In addition, the laser can be switched ('gated') on and off with a TTL gate signal. The specified power stability² of the this laser is given as 3%, which would meet our requirements. However, this specification applies to high duty cycles only. As we are working with duty cycles down to less than 10%, it is necessary to characterize the stability in this regime also. For this purpose, the laser power at several duty cycles was measured for at least 15 minutes each³. Figure 3.4 shows that there is indeed a much higher relative fluctuation present at very low duty cycles, while the specified value is already reached at 25% duty cycle. In both cases, there is a noticeable warm up period of instability which must be taken into account before starting the manufacturing procedure or after changing the duty cycle between fibers.

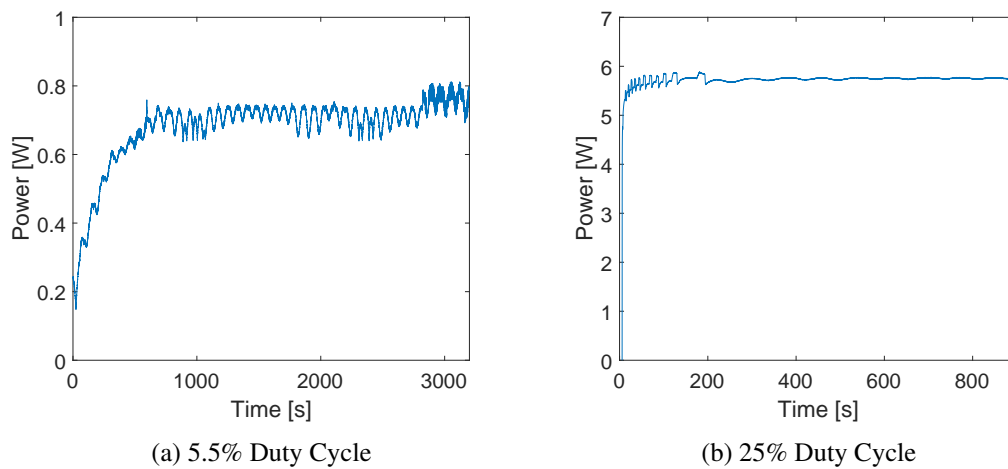


Figure 3.4: Warm up and power stability of the CO₂ laser for different duty cycles

To rule out the response of the power meter itself, or an aliasing effect between the power meter and the laser pulse repetition rate, as the source of the oscillations, a second power meter was added behind a beam splitter (see figure 3.5(a)). It showed the same power oscillation. However, at 10% duty cycle the shapes of the recorded power readings do not only deviate from each other, but even move into different directions for certain periods of time (see figure 3.5(b)). This implies jumps in mode, polarization or wavelength to which the transmission properties of the beam splitter are sensitive. Personal communication with the manufacturer did not lead to any additional information regarding the cause of this phenomenon.

To monitor the power continuously, about 0.5% of the power is coupled out onto a power sensor⁴ by an anti-reflection coated ZnSe window⁵ acting as a pick-off plate (see section 3.1.2). This beam is further attenuated such that the power sensor's dynamic range from 0 - 1 V at a sensitivity of 10 mV mW⁻¹ is spanning the full range of the laser output powers. However, large electronic noise created by the laser's power supply leads to a bad signal to noise ratio at low powers (see figure 3.6). This greatly diminishes

²Defined by the manufacturer as $\pm(P_{\max} - P_{\min})/(2P_{\max})$ at constant duty cycle after 10 minute warm-up

³using a Coherent PowerMax-Pro 150F HD

⁴Lasnix Infrared μW Power Senso Mod. 511

⁵Thorlabs WG71050-G - \varnothing 1" ZnSe Broadband Precision Window, AR Coated: 7 - 12 μm

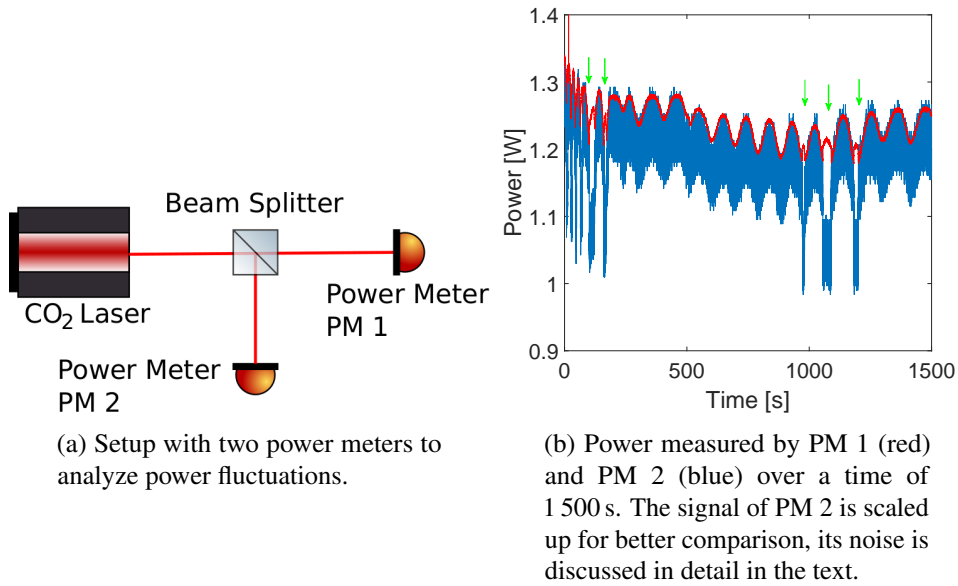


Figure 3.5: Measurement to analyze the recorded power fluctuations. As indicated by the green arrows, the signals recorded behind the two output ports of the beam splitter deviate from each other for certain periods of time.

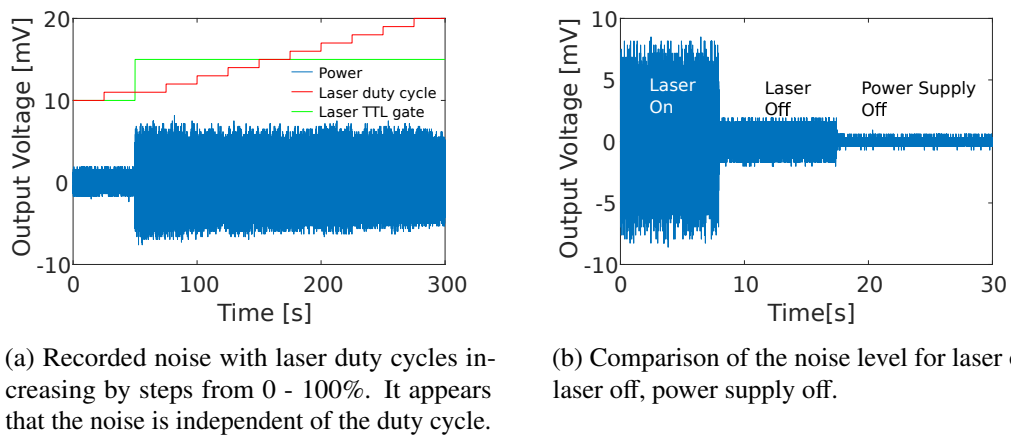


Figure 3.6: To analyze the noise of the power sensor, its output voltage was measured for different laser settings while the laser beam itself was blocked.

the reproducibility of pulses with low power. A line filter on the power strip could not solve this problem. Here, additional steps have to be taken.

The polarization of the laser is specified as $> 100 : 1$, parallel to the optical table. This has been experimentally confirmed using a linear polarizer⁶ as analyzer.

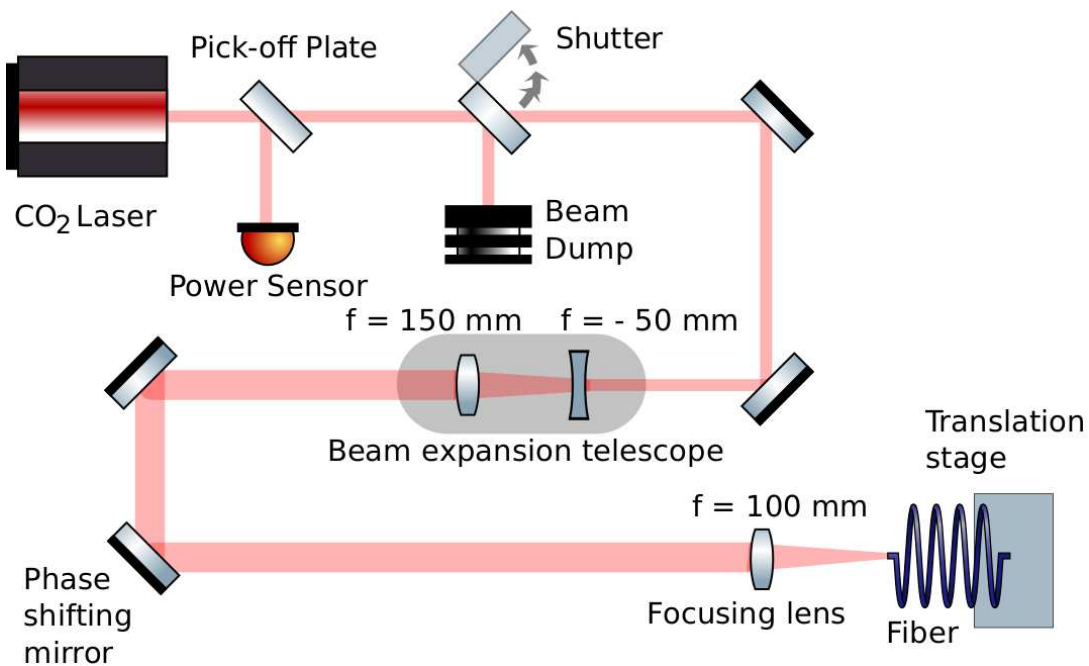


Figure 3.7: Layout of the new fiber shooting setup.

3.1.2 Optical Setup

Along its path, shown in figure 3.7, the beam passes the pick-off plate for the power sensor discussed in the previous section, a shutter (further characterized in section 3.2.3, which is reflecting the beam into a beam dump⁷, and three major beam shaping elements which will be the subject of this section: a beam expanding telescope, a phase shifting mirror, and a focusing lens. The resulting beam profile behind this last lens will be characterized in section 3.1.3.

To be able to focus the beam tightly onto the fiber tip, it needs to be expanded first. For this purpose a telescope in Galileian configuration with two ZnSe lenses with focal lengths of -50 mm and 150 mm respectively is used. Currently, it expands the beam to approximately 13 mm diameter at the position of the final focusing lens. Arranging the lenses in a cage system will allow us to change the distance between them without disturbing the rest of the alignment. Thereby, we can change the beam size and divergence, and subsequently the waist size at the fiber position, if this should be needed in the future.

In a next step, a phase shifting mirror (PSM) converts the beam from linear to circular polarization within the allowed alignment precision. Circular polarization will serve two purposes: Firstly, it will limit the mirror ellipticity caused by the polarization dependence of the ablation process, which is important to avoid the resulting frequency splitting of the polarizational eigenmodes of the cavity [27, 37]. Secondly, using circularly polarized light will prevent the formation of ripples caused by surface polaritons [38]. As seen in figure 3.8(a), the beam must impinge on the PSM with an angle of 45° between the direction of polarization and the plane of incidence. As the beam is originally polarized parallel to the optical table, this requires a second mirror to first rotate the plane of polarization, which at the same time directs the beam upwards by an angle of 45° , as depicted in figure 3.8(b). The two-mirror combination then increases the beam height by approximately 10 cm, and adds a number of alignment degrees of freedom. For this

⁶Lasnix Infrared Linear Polarizer Mod. 02

⁷Standa Water-Cooled Laser Beam Dump 10BDWC01

technical reason, perfect circular polarization has not been achieved. By inserting a linear polarizer⁸ into the beam and rotating it, the current relationship between the two directions of linear polarization was determined to be $(P_P - P_S)/P_{in} = 0.2$ (see figure 3.9). The PSM is used as the last mirror in the whole beam path to avoid further deterioration of the polarization quality by additional reflections.

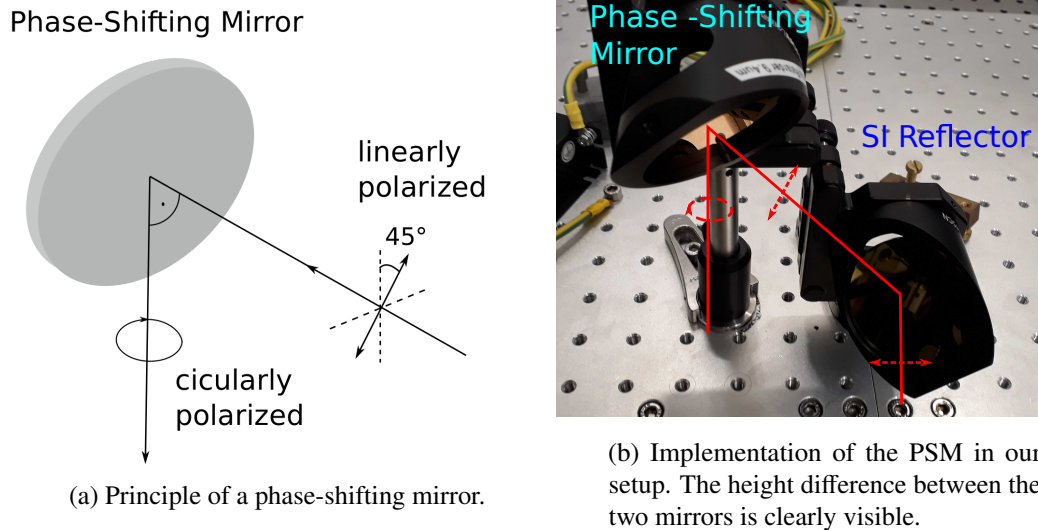


Figure 3.8: Phase shifting mirror.

Finally, a 100 mm ZnSe lens focuses the beam on the fiber tip. The originally used aspherical lens with a shorter focal length of 25 mm was removed after evaporated material was deposited on the lens surface. The fiber itself is mounted on a translation stage used to precisely position the fiber and to transport it between the laser focus and the interferometer (see section 4.2).

The alignment was carried out using thermal image plates⁹ to visualize the beam. Their surfaces contain thermal-sensitive phosphor which fluoresces when illuminated with UV-light. With increasing temperature, the intensity of this fluorescence decreases. This response to the infrared (IR) radiation of the CO₂ laser allows to identify position and shape of the laser beam falling onto the UV-illuminated plates. High sensitivity plates with low resolution allow for a coarse alignment at powers around 200 mW. Low sensitivity, high resolution plates requiring beam powers exceeding 20 W in the expanded beam were used to identify beam clipping, as they are able to resolve the resulting asymmetric diffraction patterns. Other means to visualize the beam, such as detector cards, saturate very quickly and can only be used briefly to check the beam position.

3.1.3 Beam Profiling

To profile the beam behind the focusing lens, the knife edge method¹⁰ was employed in both vertical and horizontal direction to detect asymmetries in the beam. A first series of measurements over a distance of 10 mm in steps of 0.5 mm reveals a Gaussian shape with different waist positions, sizes and angles of divergence for the two directions (see figure 3.10). In horizontal direction we find $w_0 = 44 \mu\text{m}$ and $\theta_{\text{div}} = 0.067$, in the vertical direction $w_0 = 38 \mu\text{m}$ and $\theta_{\text{div}} = 0.078$.

⁸Lasnix Infrared Linear Polarizer Mod. 02

⁹Macken Instruments Thermal Image Plate, Models 22-A and 22-B

¹⁰For more details on this method, see appendix A

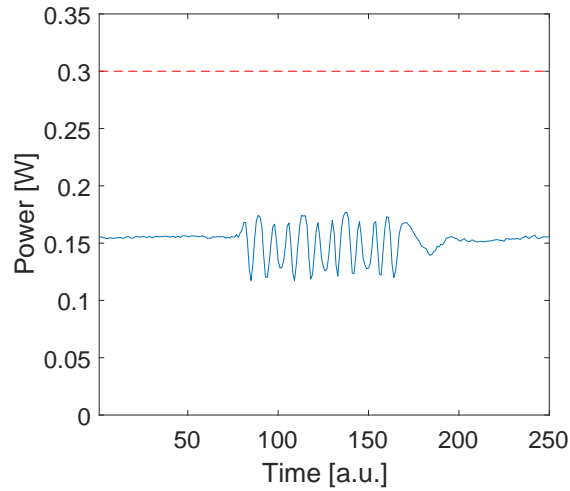


Figure 3.9: A linear polarizer was inserted into the beam ($P_{in} = 300$ mW, indicated by the red line) behind the PSM, set to $P \approx 150$ mW, and rotated several times to determine maximum and minimum transmission, corresponding to the intensities of the two orthogonal directions of linear polarization. For perfectly circularly polarized light, the transmission would be constant at $P = P_{in}/2$.

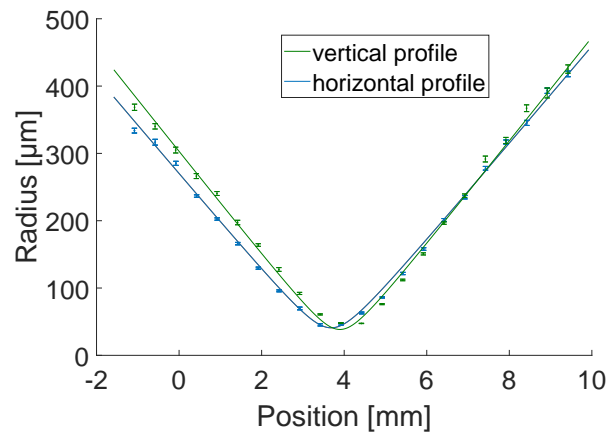


Figure 3.10: Beam profile behind the focusing lens as a function of position along the beam, measured by applying the knife edge method in both vertical and horizontal direction. The position is denoted as relative distance from the interferometer focus, the error bars indicate the 95% confidence intervals of the individual knife edge fits. An asymmetry is clearly visible

Repeating the procedure with finer steps of $100 \mu\text{m}$ around the beam waist shows that there are clear deviations from the Gaussian fitted to the coarse data. Not only do the positions of the waist not agree, but the waist sizes are also wider, $48 \mu\text{m}$ and $46 \mu\text{m}$, respectively. The latter is expected for beams which include higher order modes.

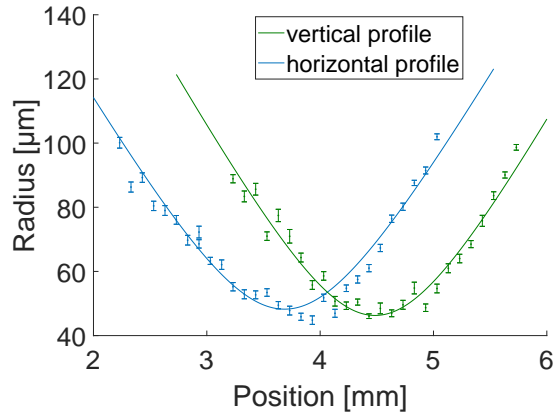


Figure 3.11: Moving in smaller steps around the waist position confirms the astigmatism and even reveals a clear deviation from an ideal Gaussian profile.

By combining this new result with the long range angle of divergence, the beam quality factors (2.13) are estimated as

$$M_{\text{hor}}^2 = 1.08 \quad \text{and} \quad M_{\text{ver}}^2 = 1.21 .$$

The laser beam quality is specified as

$$M_{\text{laser}}^2 = 1.1 \pm 0.1 .$$

Even though our results are within, or only slightly out of, this range, the disparity between the two directions suggests that additional effects stemming from the setup might play a role, causing the beam to deviate further from a Gaussian shape.

3.2 Production Process

3.2.1 Fiber Preparation

In a first step, the coating of the first few centimeters of the fibers must be removed. The fibers¹¹ used in the testing phase of the setup had an acrylate coating which could easily be removed using a standard fiber stripper. Since these fibers are not vacuum suited, they cannot be used to construct actual cavities for FCQED experiments. For this purpose, copper coated fibers¹² are required, whose coating must be etched off with an iron(III) chloride solution. In both cases the bare fiber tips must be cleaned with a solvent such as isopropanol before cleaving. The cleaving in the new setup is done with a high precision cleaver¹³ with a specified cleaving angle of $< 0.3^\circ$. This precision has largely been confirmed for this unit by a member of a different group at our university, using the cameras in a fiber splicer. The cleaving angle must be as small as possible to avoid decentration of the ablation crater. Since the diameter of the fiber core is of the order of only $5 \mu\text{m}$, small decentrations can already cause a significant drop in mode matching efficiency. As can be seen in figure 3.12, a tilt of the fiber end facet by an angle θ shifts the deepest point of the created structure by a distance $R \cdot \tan \theta$. Furthermore, the new cleaver produces

¹¹Thorlabs S630HP

¹²IVG Cu800SMF

¹³Nyfors AutoCleaver™

much flatter end facets than the previously used hand cleaver¹⁴, as shown in figure 3.13. The slight damage at the fiber edges is probably caused by an inaccurate tension setting of the cleaver. If this should cause problems, even though the damage is far way from the effective mirror, the cleaver must be reprogrammed accordingly.

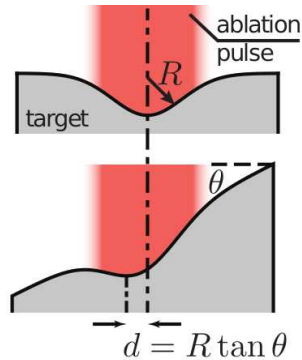


Figure 3.12: Decentration of the mirror center caused by a tilt of the fiber end facet. Taken from [30]

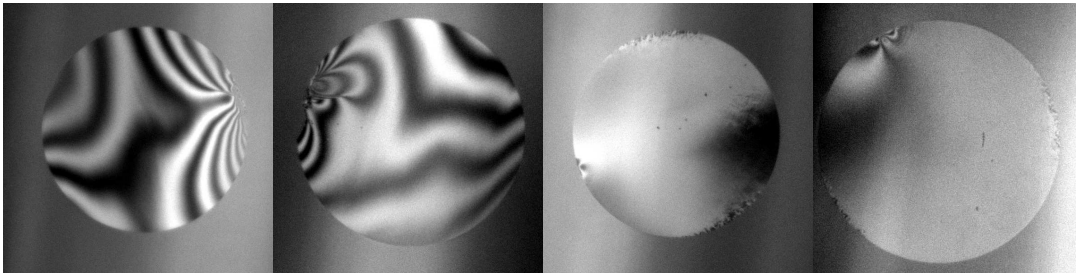


Figure 3.13: Comparison of fiber end facets (diameter 125 μm) cleaved with a hand cleaver (left, center left) and the Nyfors AutoCleaverTM (center right, right). Black and white interference fringes indicate surface unevenness, a uniformly gray area is flat. The interference microscope with which these images were taken is explained in detail in section 4.2.

3.2.2 Positioning

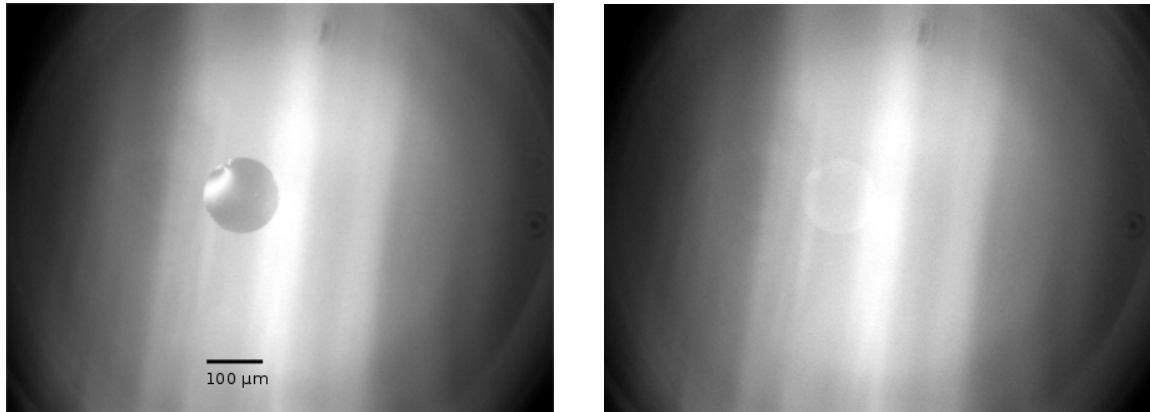
To properly position the fibers and transport them between interferometer focus and laser, we use high precision translation stages¹⁵. The first step is to mount the fiber onto the stage and bring it into the focus of the interferometer (see section 4.2). Since the coherence length of the interferometer is only on the order of about 1 μm , and the reflectivity of the reference mirror is much higher than that of the fiber tip, the fiber is only visible when positioned in a range of $\pm 3 \mu\text{m}$ around the focus (see figure 3.14). This means, even finding the fiber poses a challenge by itself and can be very time consuming. As it is not possible to mount the fiber with this degree of accuracy and reproducibility in its holder and onto the stage, the focusing procedure must be repeated for every single fiber, which poses a bottleneck for the whole process. The problem is enhanced by the fact, that the imaging system is projecting the filament of the

¹⁴Fitel model number S324 (Furukawa Electric Co Ltd)

¹⁵Aerotech ANT95-L Nanopositioning Stages

halogen bulb, leading to an inhomogeneous illumination of the interferometer's field of view. As a first step to automatize the positioning, a script was written which uses basic image processing to detect the fiber while scanning the focus along the fiber axis. However, even though it saves a significant amount of time already, in its current version it is not reliable enough to be used independently. Its success rate is still too dependent on cleaving quality and the fiber position along the other two axes. Here, it would be worthwhile to invest more time and effort into developing a more robust auto-positioning routine.

Once the fiber is properly situated in the interferometer focus, it can be transported into the correct position in the laser beam path for ablation.



(a) Fiber end facet at the interferometer focus

(b) Fiber end facet 2 μm out of focus

Figure 3.14: View of the fiber end facets on the interferometer screen. It is obvious that a defocussing of as little as 2 μm makes it already hard to see the fiber. The pattern of light and dark stripes is a projection of the light bulb's filament.

3.2.3 Ablation Sequence

After the fiber is in place, and power and pulse duration have been set, the ablation sequence itself can be started. It is a fully automatized procedure consisting of the following steps: First, the laser is switched off while the shutter is being opened. Then the laser is switched back on for the preset pulse duration. It stays off while the shutter is closing again and it is finally switched back on after the shutter is closed completely. In order to keep the laser in thermal equilibrium, the off-time should be kept as short as possible. To optimize the sequence, the response and rise time of the shutter needed to be determined. For this purpose, a power meter was placed behind the initially closed shutter, and the power was recorded as a function of time after the shutter was triggered to. As can be seen in 3.16(a), the response and rise times are 50 and 20 ms, respectively, which is an order of magnitude longer than the shortest typical ablation pulse lengths. Figure 3.16(b) shows the same sequence with the laser being gated off for the shutter movements. The power overshoot at the beginning of the laser pulse warrants further investigations to determine if the sequence can be improved by delaying switching off the laser to a moment within the shutter response time. A series of measurements with different off-times, powers and pulse durations has shown, however, that this overshoot starts occurring after off-times as short as 5 ms, which is shorter than the rise time of the shutter (see figure 3.17). We must conclude that with the current shutter, there is no way to avoid this overshoot. The laser power returns to its equilibrium value after approximately 10 ms,

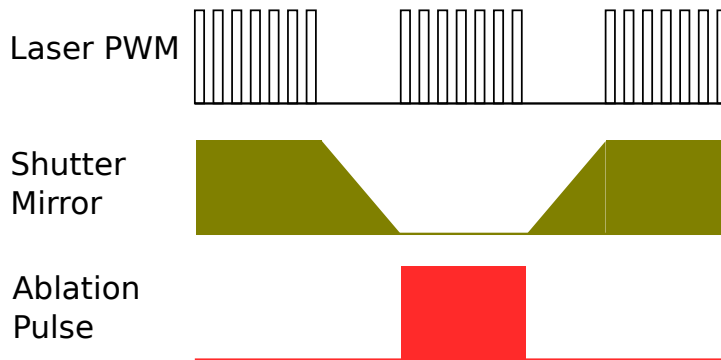
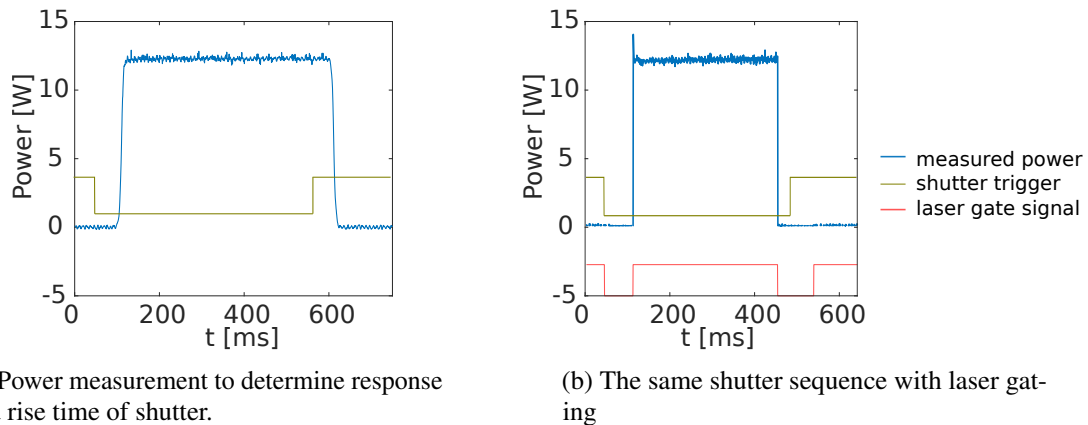


Figure 3.15: Temporal sequence for the generation of an ablation pulse with laser drive signal, shutter position, and pulse reaching the fiber position.



(a) Power measurement to determine response and rise time of shutter.

(b) The same shutter sequence with laser gating

Figure 3.16: The laser power behind the shutter was measured after opening and closing the shutter to determine the response and rise time of the shutter and to characterize the laser behavior when being gated off during the shutter movements.

meaning that the power mismatch between the set power before the pulse and the pulse power itself is most pronounced for very short pulses. One way to compensate in this case would be setting the laser to an equilibrium power that is lower than the desired pulse power.

The plan to use a high speed shutter¹⁶ was abandoned after our unit did not meet the manufacturer's power specifications of 50W, but its mirror was destroyed by a beam with a power of around 1W. The mirror of the replacement unit looked similarly dirty and fragile. It is worth noting that already very small pieces of dust or other dirt can absorb enough heat from the CO₂ laser to melt through mirror coatings, damage the substrate, and completely destroy thin mirrors such as the one inside the high speed shutter.

3.2.4 Control

All devices used in the ablation and analysis procedures are interfaced with the lab computer. From here, the whole process is controlled via a self-written Matlab graphical user interface (GUI) (see figure 3.18)

¹⁶Standa Ultra-Fast Motorized Laser Beam Shutter 10FBS-40-25-9300-C

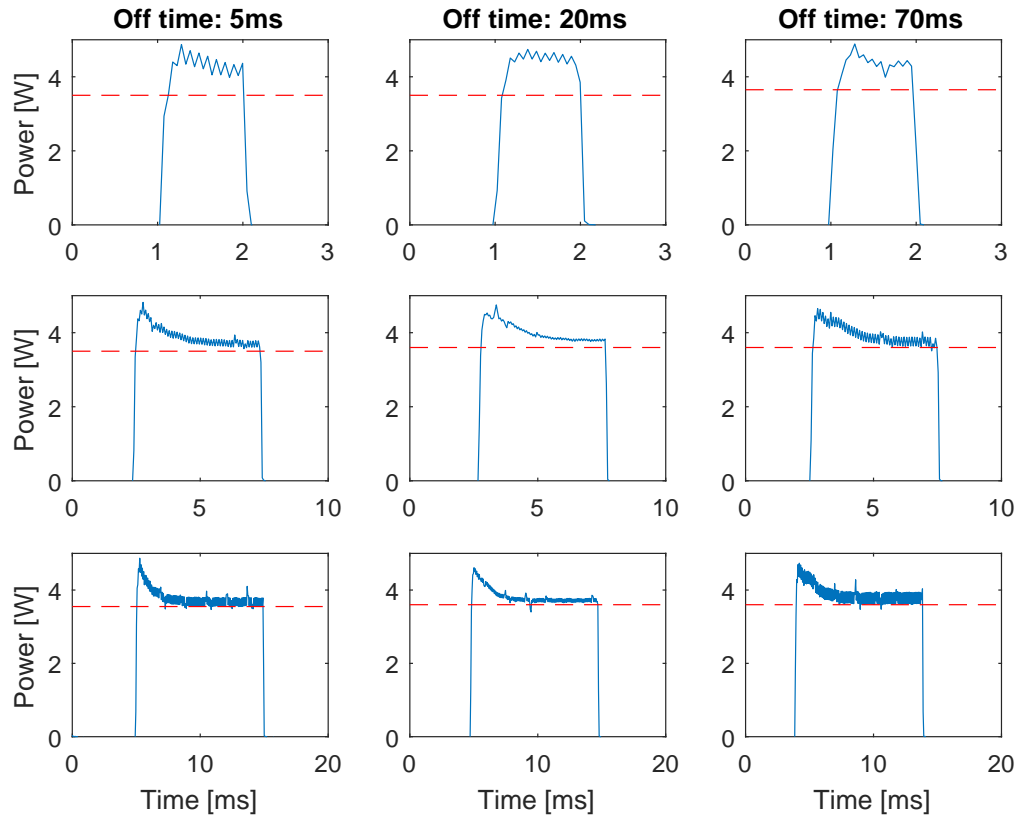


Figure 3.17: Pulse shapes for different pulse durations (1 ms, upper row, 5 ms middle row, 10 ms bottom row) and off-times of the laser at a duty cycle of 12%. The red line indicates the laser power before the laser was gated off. It can be seen that there is already a power overshoot at gating times as short as 5 ms. Also, there is no substantial difference between the currently used off time of 70 ms and the pure rise time of the shutter of 20 ms. The short term oscillations appear to be an aliasing effect between the sampling rate of the power meter and the PWM frequency of the laser. They are also visible when the laser is in equilibrium (not shown here).

which also includes access to the analysis routines. Both, the translation stages and the piezo focusing (PIFOC) stage of the interferometer are connected via USB and controlled using Matlab drivers provided by their respective manufacturers. The communication with the camera is based on Matlab's image acquisition toolbox. Power sensor, interferometer illumination, and all signals going to and coming from the laser are interfaced via a National Instruments input/output card¹⁷ connected to a BNC adapter block¹⁸.

The GUI's layout (see image 3.18) can be divided in five parts: The upper left part controls the translation stages. The lower left part controls the laser and ablation sequence. Here, laser duty cycle, pulse duration and number of pulses are set, and the sequence is triggered. The upper right part contains the several analysis methods. Here, especially direct access to the brightest pixel method is useful to analyze fibers on the fly. Also including the other more detailed methods here leaves the possibility to fully integrate experimental control and analysis. This integration would allow direct feedback to modify positioning and ablation parameters automatically, based on the results of previous fibers. While this has not been implemented yet, this option was one of the reasons to combine control and analysis software. The middle right part of the GUI controls the interferometer. It allows to individually control the PIFO stage, the camera and the halogen bulb and to set an automatic interferometry sequence with flexible step sizes and number of images. The interferometer control is implemented such that there is no direct dependence on an ablation sequence. This means the GUI can also be used to control the interference microscope for other purposes than profiling fiber end facets. Similarly, the analysis routines are split into two separate parts: pure surface reconstruction on the one hand, and fitting procedures assuming a near Gaussian depression on the other hand. To profile other objects, one can still use the first part and then process the surface reconstruction with own routines, custom made to suit the task at hand. Lastly, on the bottom right, there is a number of status indicators for the laser and the connected devices. It also allows to retry failed connection attempts without having to restart the program after solving the responsible problem.

¹⁷NI PCIe-6321

¹⁸BNC-2110

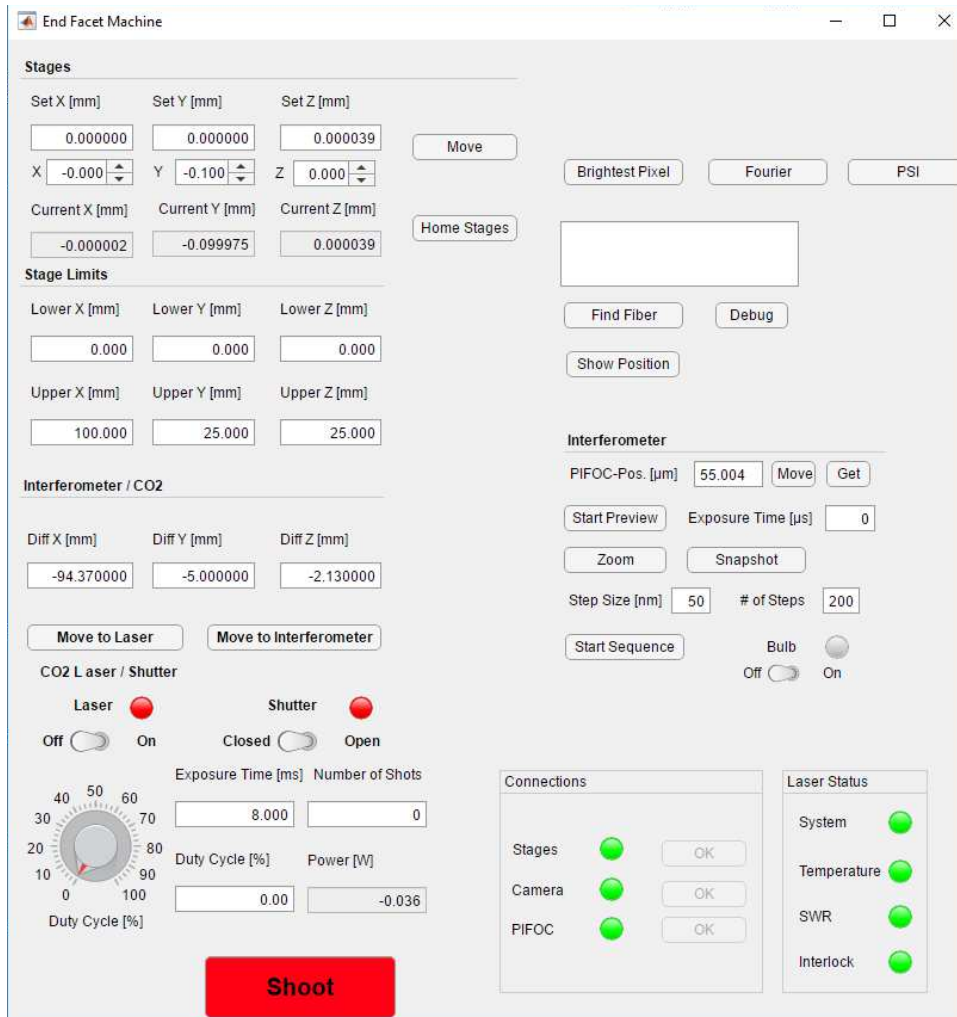


Figure 3.18: Screen shot of the graphical user interface used to control the shooting sequence and analyse the results.

Surface Profiling

In order to reconstruct the 3D-surface of the fiber end facets, we use white light interferometry (WLI) with a Mirau objective. In this chapter I will introduce the principles of WLI (section 4.1), describe our Mirau interferometer (section 4.2), and compare our analysis methods (section 4.3).

4.1 White Light Interferometry

To profile surfaces with interferometric methods, the object of interest is illuminated with a light source, the reflected light is superimposed with a reference beam, the object is moved along the direction of the light beam, and the resulting intensity pattern is recorded as a function of position. For a monochromatic light source with wavelength λ , the resulting intensity for each point on the surface is given by

$$I = I_0 + I_m \cos(\varphi), \quad (4.1)$$

with background and modulation intensities I_0 and I_m respectively. The phase φ is a function of the height of this point on the surface with

$$h = \frac{\varphi}{4\pi} \lambda. \quad (4.2)$$

However, the phase ambiguity $\varphi \in [0, 2\pi]$ leads to a height ambiguity, necessitating further phase unwrapping techniques.

For polychromatic light, equation 4.1 is modified by a visibility or coherence envelope function V to

$$I = I_0 + I_m V \cos(\varphi) \quad (4.3)$$

Here, the height is given by the position of the maximum of this envelope [39]. In this position, the optical path difference (OPD) between object beam and reference beam is exactly zero. Therefore, using white light instead of a monochromatic or narrow band source, and scanning the surface over a distance of several coherence lengths to find this maximum for every point, offers an additional piece of information to extract the surface profile. For an idealized white light source with a Gaussian spectral distribution the coherence envelope is again a Gaussian. The recorded intensity at each position on the surface as a function of position is then given as

$$I(z) = I_0 + I_m \exp\left[-4\left(\frac{z - z_0}{l_c}\right)^2\right] \cos\left(4\pi\frac{z - z_0}{\lambda_0} - \varphi_0\right) \quad (4.4)$$

with coherence length $l_c = \frac{c}{\pi\Delta\nu}$ and central wavelength λ_0 . z_0 is the position of zero OPD, i.e. the relevant parameter indicating the relative height of each point on the surface. Determining its value for every point yields a full surface reconstruction.

4.2 Mirau Interferometer

To record the necessary interferograms we use a Mirau interferometer whose setup is sketched in figure 4.1. As a white light source we use a halogen bulb (see section 4.2.2). A beam splitter directs the light into an infinity corrected Mirau objective¹ (see section 4.2.1). The reflected beam is then focused by a 200 mm tube lens onto an 8MP CCD camera². The surface of the fiber end facet is scanned by moving the objective by 200-300 steps of 40-50 nm, using a piezo focusing stage, and recording an image for each step. Three typical images of one such series are shown in figure 4.3. The exact number of steps and their distance depends on the surface depth and can be chosen independently for each measurement. These image series result in an interferogram $I(z)$ for each pixel, with I being the pixel brightness and z the frame number of the raw data. To reconstruct the height, z must be converted into units of distance, the intensity can remain in arbitrary units, since we are only interested in relative intensity differences.

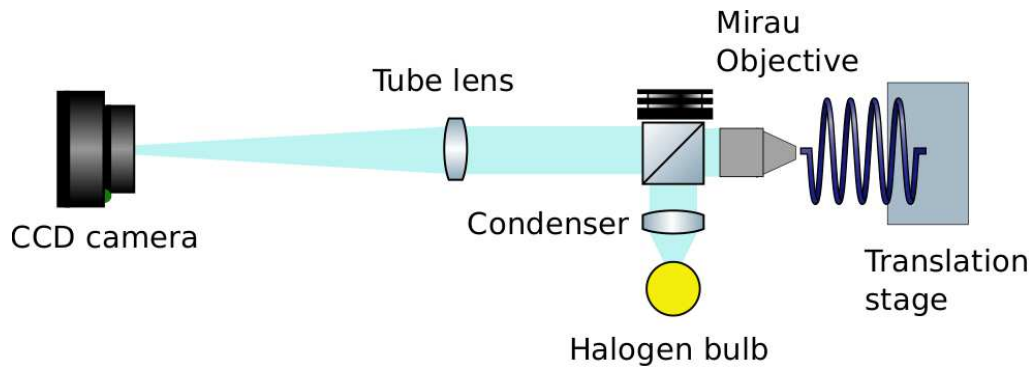


Figure 4.1: Sketch of our Mirau interferometer.

4.2.1 Mirau Objective

A Mirau objective is a microscope objective with a built in reference mirror to create an interference pattern (see figure 4.2). When the surface being investigated is in the focal plane, the optical path difference between object beam and reference beam is zero and the two beams interfere constructively. For positions away from the focus, typical interference fringes appear, whose contrast decreases with distance until the object is out of the coherence region. Figure 4.3 shows the central part of a fiber end facet with a circular depression at three different distances from the focus of such an objective. In the first frame the edge of the crater is in the focal plane, in the second and third image this is true for the sloped part and the bottom respectively. From the relative position difference between the first and the last frame, one can already infer the height difference between edge and bottom of the depression. The change in fringe pattern from frame to frame can be used to reconstruct the whole surface.

¹Nikon CF Plan DI20X, EPI (NA:0.40, WD:4.7mm)

²Thorlabs 8051M-USB

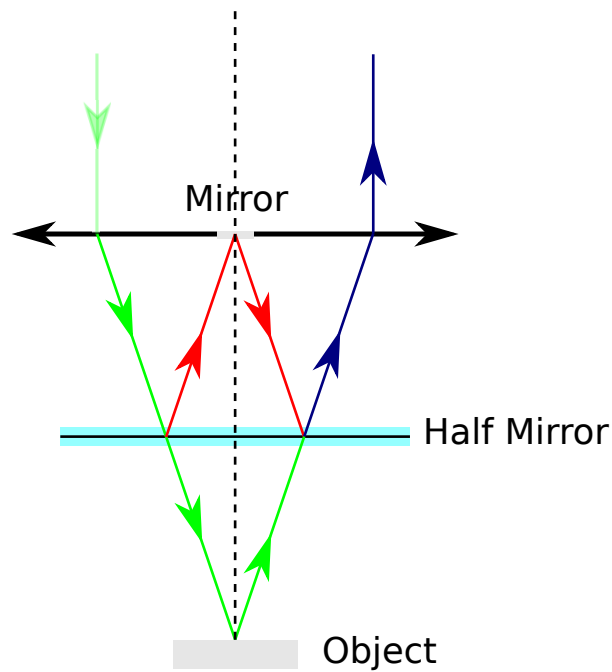


Figure 4.2: Principle of a Mirau objective. The object beam (green) interferes with the reference beam (red). As long as the optical path difference is within the coherence length, the resulting beam (blue) exhibits a fringe pattern [40].

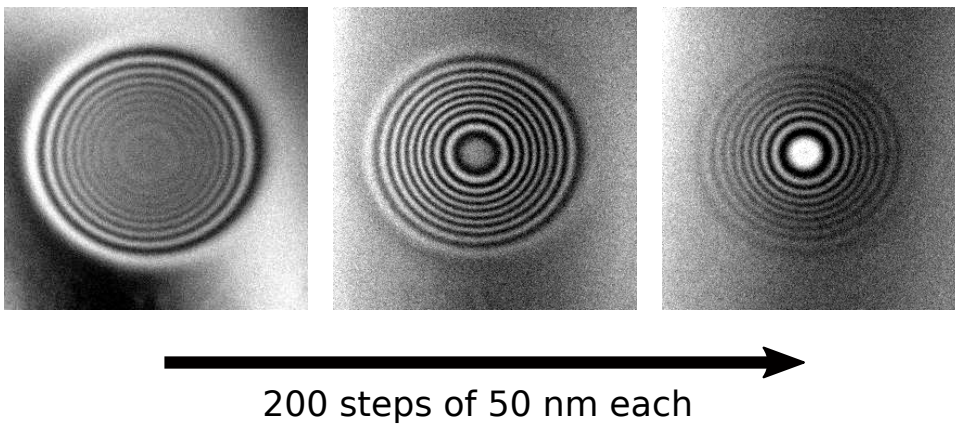


Figure 4.3: Three frames of a series of interferometer images. The shift of the maximum brightness and contrast as a function of z-position can clearly be seen.

To move the Mirau objective, we use a piezo focusing stage³ with a capacitive sensor. Its closed-loop positional stability (see figure 4.4) is an order of magnitude smaller than the typical step size of 40-50 nm in an interferogram sequence.

³PI Piezo Focusing Stage P-721, controlled by a PI E-709 controller

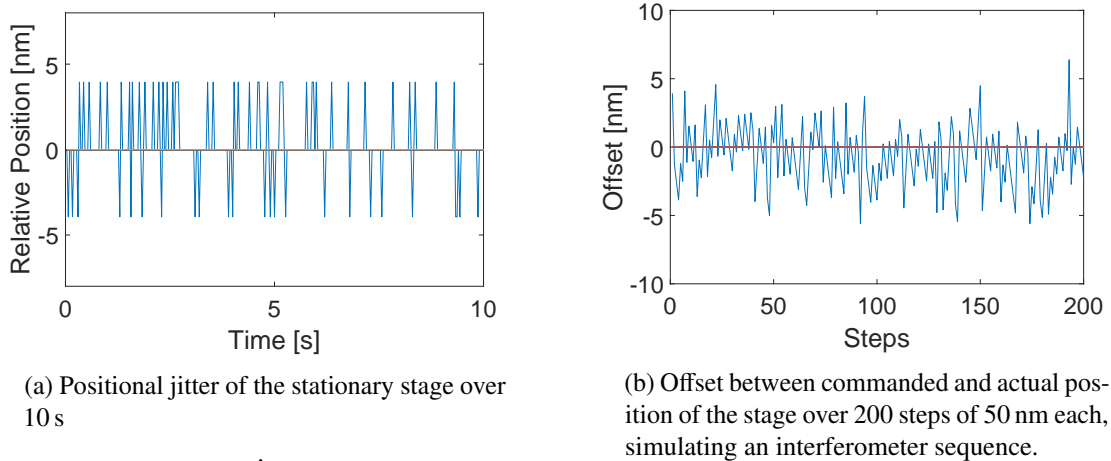


Figure 4.4: Accuracy of the Mirau objective's piezo focusing stage. The positional information was recorded using the internal capacitive sensor of the stage.

4.2.2 Illumination

For illumination we use an Osram 64265 HLX halogen bulb. Even though it is specified for a maximum of 30W, for our purposes it can only be used at up to 15W to prevent detrimental thermal effects which occur at higher powers: The heat generated by the bulb then causes fluctuations of the interferograms on sub-second time scales, reducing the accuracy of the analysis. On time scales of the order of minutes, thermal expansion of the interferometer would shift the position of the focal plane. Since the location of the fiber end facet in the laser beam is most easily measured relative to the interferometer focus, this effect reduces the reproducibility of this position. The conclusion that this drift is caused by the bulb, and not by other instabilities, is supported by the observation that switching off the bulb for an hour brings the focus back to its original position.

An additional effect of using this bulb is inhomogeneous illumination. It is caused by the imaging of its filament onto the interferometer's focal plane. A first attempt to improve the situation with a diffuser was unsuccessful. Using a custom made bulb holder from our mechanical work shop improved the situation, but taking further steps might improve the quality of the interferograms.

4.3 Analysis Methods

To analyze the interferograms obtained by this Mirau interferometer, three different methods with varying accuracy and computation times have been tested. In the first two, the maximum of the visibility function was approximated to different degrees of accuracy, while disregarding the fringes resulting from the cosine part of the intensity modulation. In a third method, the phase information of these periodic fringes was extracted and unwrapped to reconstruct the surface. Results, advantages, and disadvantages of these methods will be discussed in the following sections. A full 201-frame, 50 nm-step interferometry sequence of the central part of the machined fiber end facet seen in figure 4.5 is used as an example.

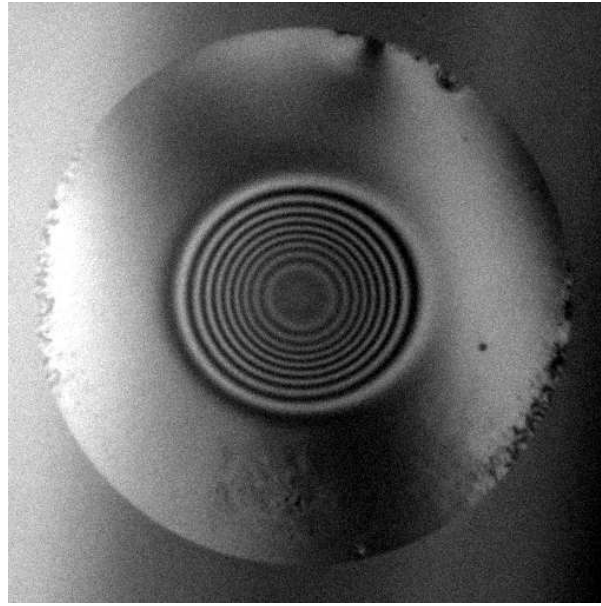


Figure 4.5: Fiber tip (\emptyset 125 μm) with ablation crater. The ablation parameters were $P = 1.1$ W, $t = 3$ ms, $w = 67$ μm .

4.3.1 Brightest Pixel Method

This is the fastest but also the most coarse method. It makes the approximation, that the position of the frame with maximum intensity for a given pixel coincides with the maximum of the visibility function [41]. As a consequence, the resolution is limited to the step size of the interferograms. Furthermore, depending on the relative position of the fringe maxima with regard to the envelope and depending on the sampling positions, the brightest pixel might belong to a different peak than the one closest to the maximum. The uncertainty resulting from this effect corresponds to the distance between two interference maxima, i.e. $\lambda_0/2$, where λ_0 is the effective wavelength. Experience shows, that positions near steep slopes can lead to even higher deviations. Examples for these cases can be seen in figure 4.6. The resulting surface reconstruction for our example fiber is shown in figure 4.7.

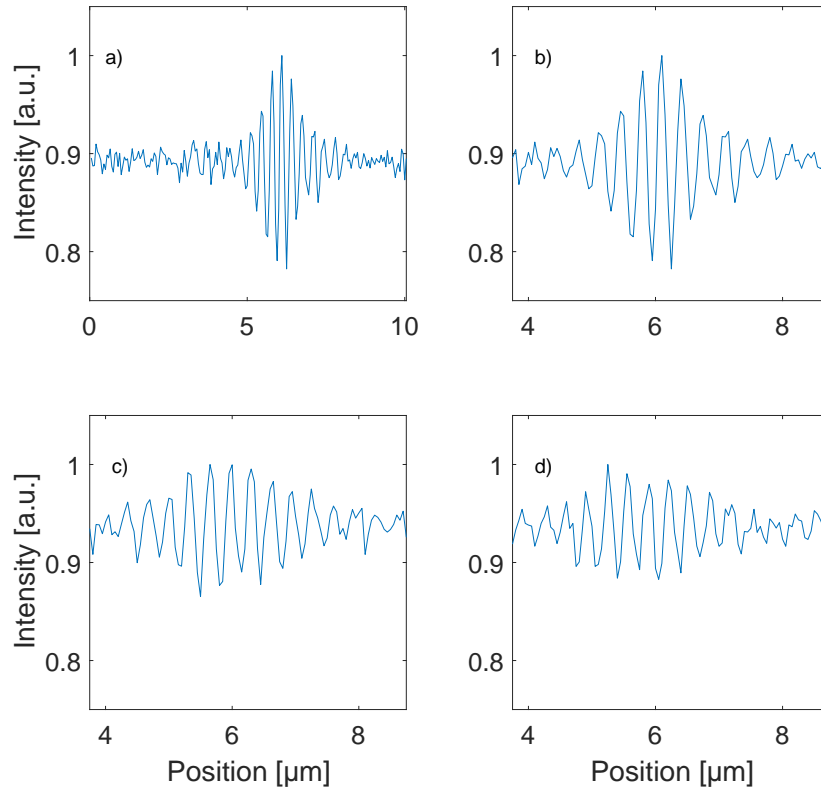


Figure 4.6: Interferograms for three different pixel positions. a) shows the full interferogram for a pixel near the center. b) shows the relevant central part of the fringe pattern for the same pixel. It is clearly visible that the peak of the brightest fringe is near the center of the envelope. c) shows a fringe pattern where the two brightest peaks have almost the same size. In this case noise or sampling position can be a decisive factor for the brightest pixel. d) shows an example of a position at a steep slope. Here, the brightest pixel is obviously far away from the center. For pixels like this, the brightest pixel method fails.

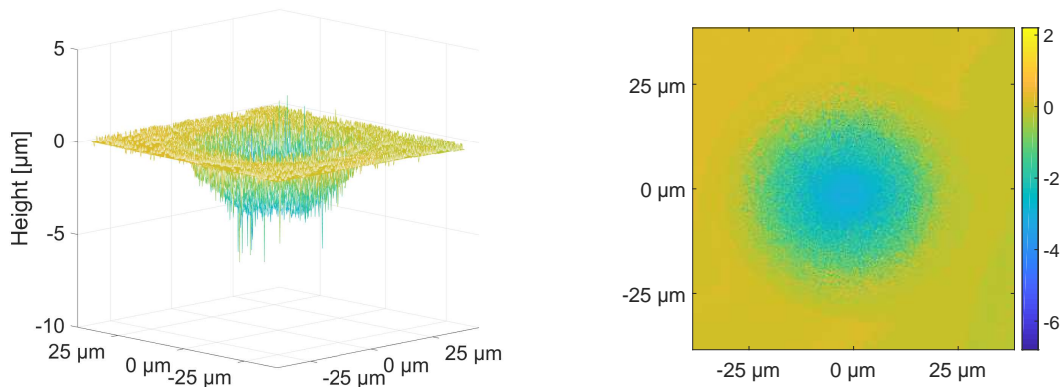


Figure 4.7: The reconstructed surface using the brightest pixel method shown in 3D and 2D. It is clearly visible that the problem with pixels on steep slopes is a systematic one and not unique to the pixel presented above. The computation time was about 2 s.

4.3.2 Fourier Analysis

This smoother but also more computation time intensive method uses Fourier analysis to extract the envelope function from the interferograms. Here, the Fourier transform of the interferogram is taken and filtered to keep only the positive frequency components contributing to the envelope. Inverse Fourier transform then returns the envelope (see figure 4.8). For the mathematical details refer to [42]. To extract the height information, the maximum of this envelope must be determined. In the ideal case of the Gaussian spectral distribution described above, this could easily be achieved by fitting a Gaussian to the envelope. However, compared to a Gaussian, the spectrum of our light bulb is weighted heavily to the red. This effect is increased by the necessity to dim down the bulb. Additionally, the exact shape of the interferogram can vary significantly from pixel to pixel. Despite of this, a Gaussian approximation still yields a smoother surface (see figure 4.9) that appears to be in agreement with the results of the other methods. This smoothness makes it easier to fit parameters such as the radius of curvature, but without independent calibration it is not possible to say with certainty that these results are more accurate than those of the faster method. It is therefore doubtful that the long computation time, 260 s in this example, is currently justified. Filtering the light source to achieve a more Gaussian spectral distribution and taking steps to increase the fringe contrast might improve this situation. Fitting a higher order polynomial

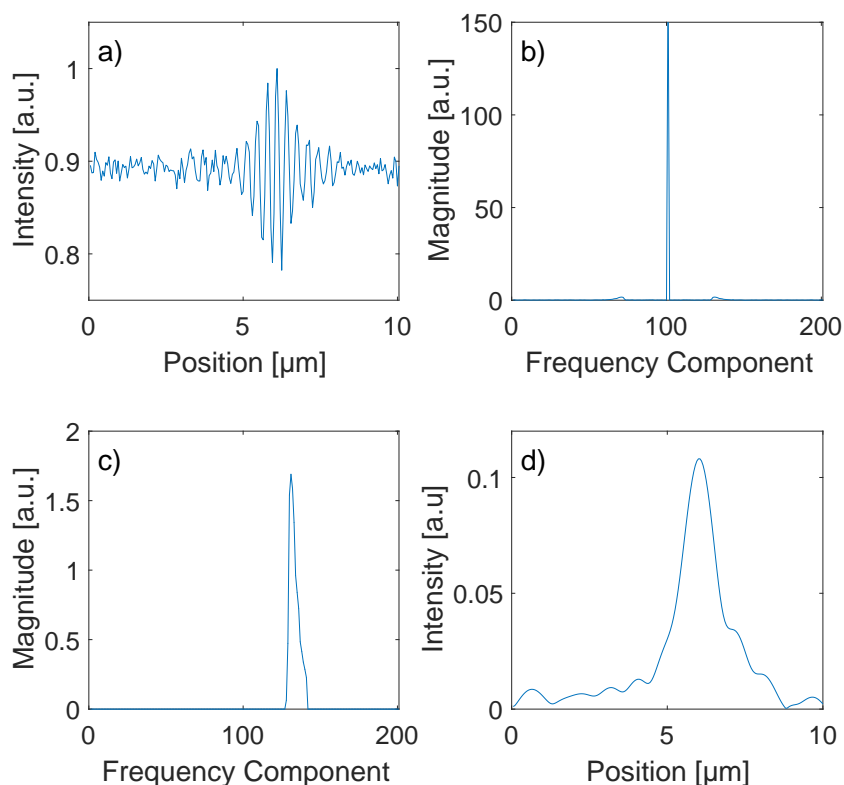


Figure 4.8: Principle of the Fourier analysis method: a) shows again a single pixel interferogram. The other images show: b) its Fourier spectrum, c) the filtered frequency package in the Fourier domain containing the envelope and d) the extracted envelope. For the last image, the frame steps have already been converted into units of distance.

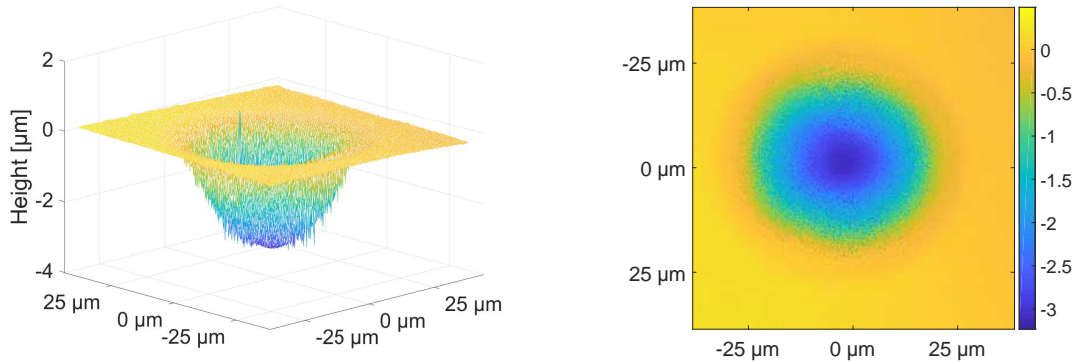


Figure 4.9: The reconstructed surface using the Fourier analysis pixel method shown in 3D and 2D. The result is smoother, but the inaccuracies occurring at steep slopes are still visible. The computation time was 260 s.

instead of a Gaussian is much faster, but leads to faulty results if the apparent envelope has two local maxima. This again is an effect observed for pixels on steep slopes. For cleaner interferograms this method exhibits a very good ratio between computation time and result for the maximum of the envelope. Apart from improving the contrast, optimizing the sampling rate could result in more accurate envelopes. A higher sampling rate would however mean significantly more data to be recorded and processed. Here again, it is necessary to investigate if the additional processing time is justified.

4.3.3 Phase Unwrapping

Unlike the previous methods, this approach uses the phase information. By fitting a cosine wave modulated with a Gaussian envelope to the central part of the fringe pattern, a phase map is created (see figure??). This phase map can then be unwrapped with the Costantini algorithm to extract the surface information [43]. Here again, we make the approximation of a Gaussian spectral distribution. Since we are only interested in the properties of the cosine part of the function, and we are only fitting to the central part of interferogram, the exact shape of the envelope does not play a role and the approximation is justified. The width of the Gaussian in each case can therefore be left as a free parameter.

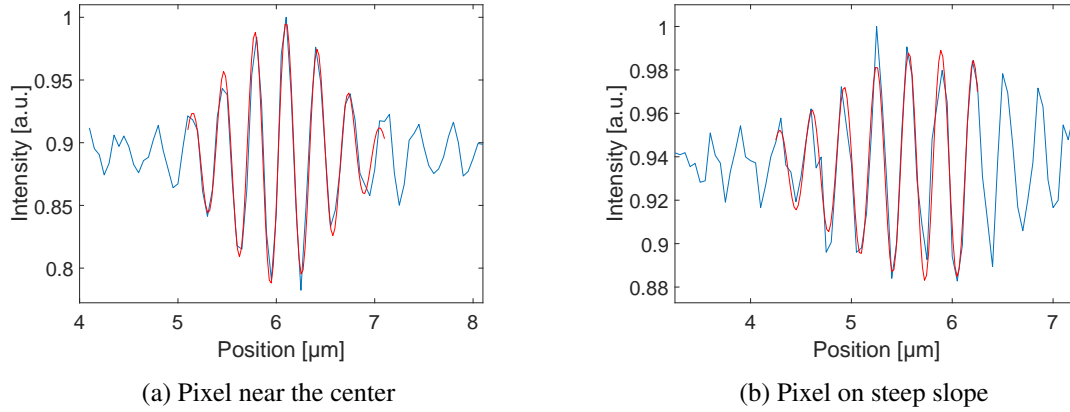


Figure 4.10: Central parts of the recorded fringe pattern (blue) with the corresponding fits to determine the relative phase (red). As seen in (b), also the interferograms that are useless for the brightest pixel analysis method yield good phase information, even though the fit is not centered, because the fit window is chosen as centered around the brightest pixel.

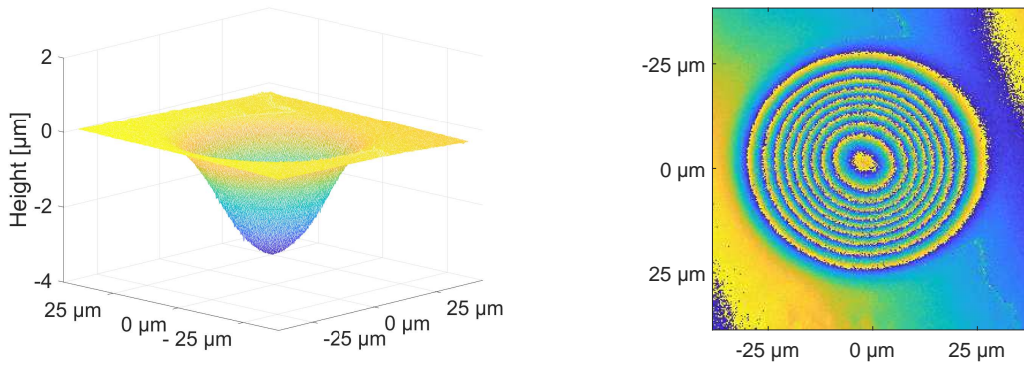


Figure 4.11: The reconstructed surface using the phase unwrapping method and the corresponding phasemap. As expected from the interferogram in figure 4.10(b), the steep slope does not cause a problem here. The computation time of 532 s was twice as long as for the previous method.

4.4 Radius of Curvature Extraction

As the model in section 2.2 predicts an approximately Gaussian shape of the resulting structure, we fit a 2D-Gaussian to the full surface extracted in section 4.3.3. As can be seen in figure 4.12, the prediction is not perfectly fulfilled. This is not unexpected, considering the large number of approximations made. Especially the non-linearity of the thermal conduction coefficient and the geometric boundary condition of the fiber predict a flatter temperature profile and therefore a larger structure diameter than the simple Gaussian model [32]. The deviation between the actual shape and a Gaussian over the whole structure is particularly large near the center. Since this is the area of the effective mirror, we need to restrict our fits to this central area to determine values for the mirror radii of curvature. Figure 4.13 shows Gaussian and spherical fits to this inner region. The radius of curvature for the Gaussian fit is calculated as $R_{\text{Gauss}} = \sigma^2/a$, where a is the amplitude [14]. It is apparent that there is a discrepancy between the results for the two fit functions. Experience with the old setup showed, that in this case the spherical

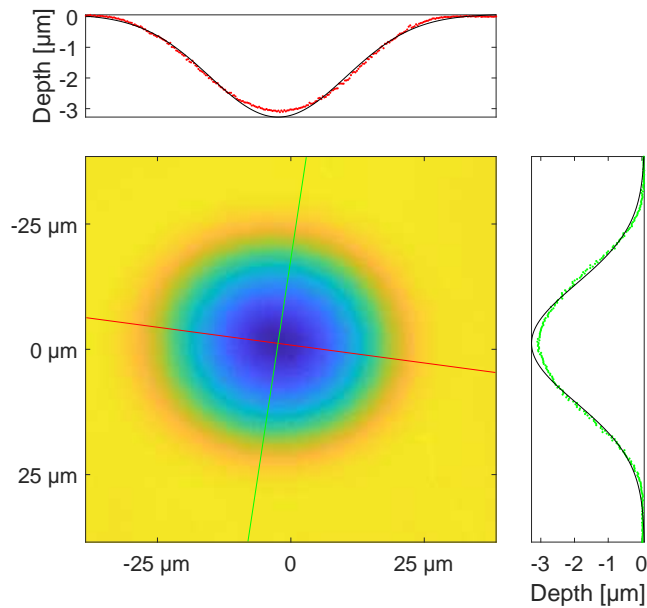


Figure 4.12: Gaussian fits through the major and minor axes of a 2D Gaussian fitted to the full surface from section 4.3.3. It reveals that the depression does not have a perfectly Gaussian shape. The deviation is especially strong near the mirror center.

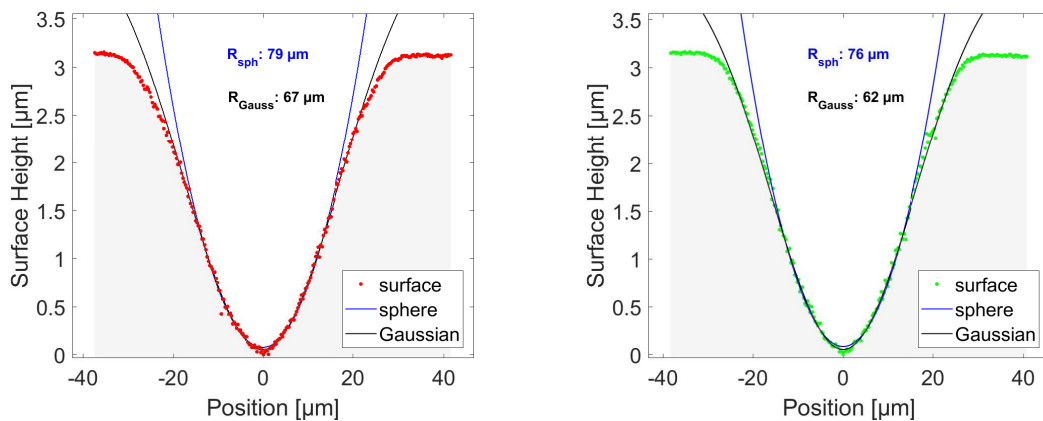


Figure 4.13: Gaussian and spherical fits restricted to the central part of the same cross sections as in figure 4.12

fit result came closer to the experimentally measured value for the effective radius of curvature. In that case, however, the radii of curvature were typically of the order of $\sim 170 \mu\text{m}$, i.e. more than twice as large as in the case of this test fiber [18]. The fitting results for the radii of curvature for this surface are summarized in table 4.1.

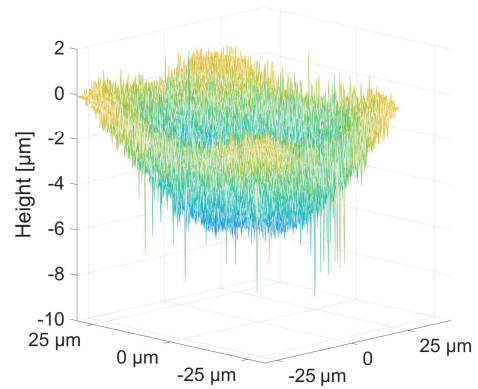
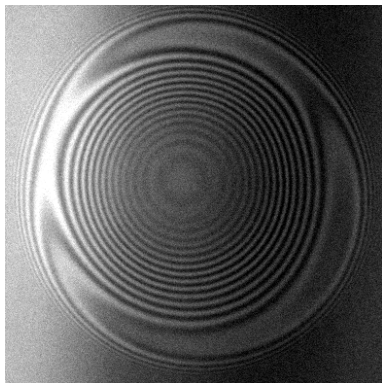
Method	red cross-section		green cross-section	
	$R_{\text{sph}}[\mu\text{m}]$	$R_{\text{Gauss}}[\mu\text{m}]$	$R_{\text{sph}}[\mu\text{m}]$	$R_{\text{Gauss}}[\mu\text{m}]$
Brightest Pixel	112	72	76	74
Fourier Analysis	83	66	66	38
Phase Unwrapping	81	68	77	63

Table 4.1: Comparison of the different fit results for the radii of curvature. It is apparent, that for the red cross section Fourier analysis and phase unwrapping are in good agreement, while the brightest pixel method results yield larger values, especially for the spherical approximation. For the green cross section, however, the value resulting from Fourier analysis disagree with the others.

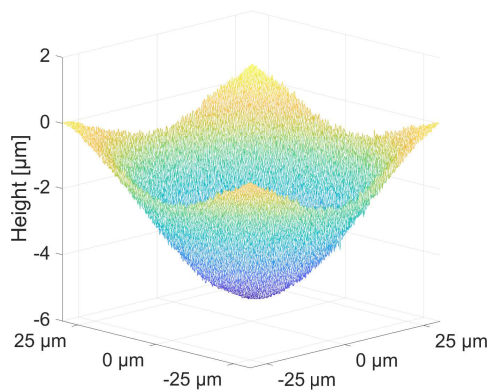
4.5 Comparison

The data in table 4.1 shows, that there are large discrepancies between the results of the different analysis methods. In particular, the relative agreements between the methods vary for both cross-sections. For the one indicated in red, Fourier analysis and phase unwrapping yield very similar values. For the green cross-section the brightest pixel agrees better with phase unwrapping, while the Fourier analysis appears to be an outlier. The smoothness of the surface reconstruction, and the fact that in each of the fits one other method supports its result, suggest that the phase unwrapping algorithm delivers the most accurate results. It is worth noting, however, that in other instances it fails completely. One such example can be seen in figure 4.14. Here, the central part of a large ablation crater, spanning almost the whole fiber end facet, was profiled. In this case, the Fourier analysis yields the smoothest reconstruction while the phase unwrapping algorithm returns a surface with large discontinuities. Therefore it is important to have more than one accurate technique available. As soon as more data has been collected, it might be possible to predict the method best suited for the different structure shapes or sizes. Furthermore, these examples show that currently the brightest pixel method is not reliable enough to take advantage of its speed to analyze fibers on the fly. One has to conclude, that it is not possible yet to deliver a definite verdict, before the effective radii of curvature have been independently determined experimentally.

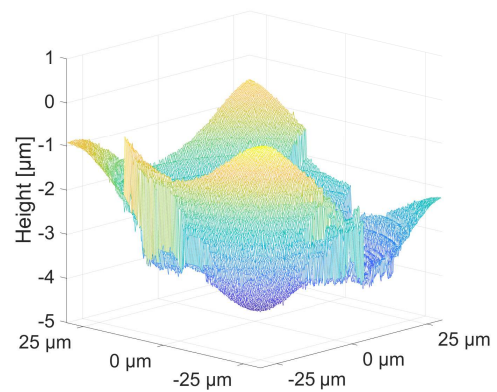
At this point, working principles have been given and compared. More rigorous analysis is required once more data is available.



(a) Brightest pixel method



(b) Fourier analysis method



(c) Phase unwrapping method

Figure 4.14: Direct comparison of the three surface reconstructions of one fiber in a case in which the phase unwrapping method fails.

Results

In the following two sections, I will briefly present the first preliminary data relating the shape of the ablation craters to different pulse parameters. Those were power, pulse length, and position along the beam axis. i.e. effective beam diameter. In light of the results from the previous chapter, the phase unwrapping method was used to reconstruct the surfaces. For most of the ablation craters analyzed so far, it yielded a smooth shape. Structures for which this method failed were discarded here to maintain a better comparability of the results.

5.1 Radius of Curvature

The first sample to be machined and properly analyzed was a 1 mm thick UV fused silica window¹. Because of its size it was possible to create a large series of ablation craters with different parameters without having to mount and position a new fiber for each pulse. This is especially advantageous when sweeping through a new parameter set. In these cases it might take several test pulses to find a parameter regime in which useful structures are created. Useful structures in this case refers to concave structures with a size in and around the same range as desired fiber mirrors. Since the material of the fused silica window is very similar to that of fibers, the results offer good starting points for similar parameter sweeps on fiber end facets. The exact results for fibers are expected to differ slightly, due to the different geometrical boundary conditions for the heat transfer and due to the doping of the fiber.

It can be seen in figure 5.1 that the expected result for the relationship between radius of curvature and structure depth for craters carved by CO₂ laser pulses [14] is observed. This is an indication that the new setup is working as predicted and that this analysis procedure is reliable.

5.2 Eccentricity

The number of machined fibers has not yet been large enough to present parameter comparisons such as in the section above, but it has been useful to investigate the eccentricity of the mirror structures. This eccentricity is defined as [27]

$$\epsilon = \sqrt{1 - \frac{R_1}{R_2}}, \quad (5.1)$$

¹Thorlabs WG41010R - 25 mm x 36 mm UVFS Broadband Precision Window

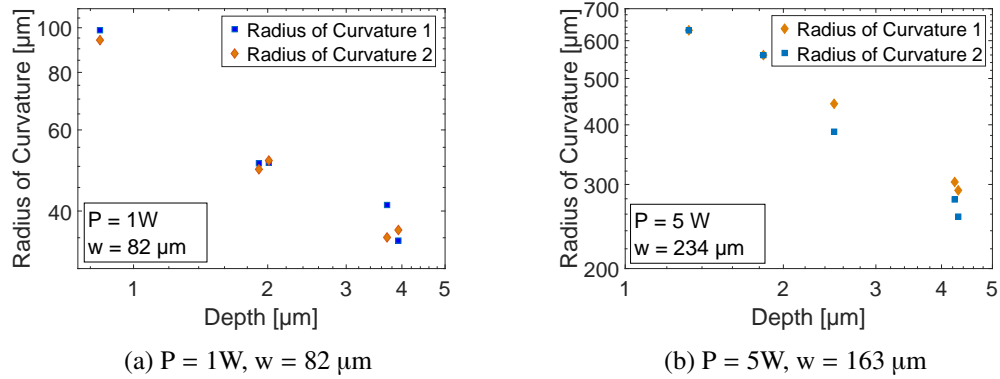


Figure 5.1: Relationship between structure depth and radius of curvature for different pulse lengths. On a double logarithmic scale a linear behavior is expected for pulses of equal power and width

where R_1 and R_2 are the radii of curvature along the major and minor axis of the fitted 2D Gaussian respectively. Plotting these values against the angle ϕ between the major axis and the horizontal reveals a preferred axis of eccentricity (see figure 5.2).

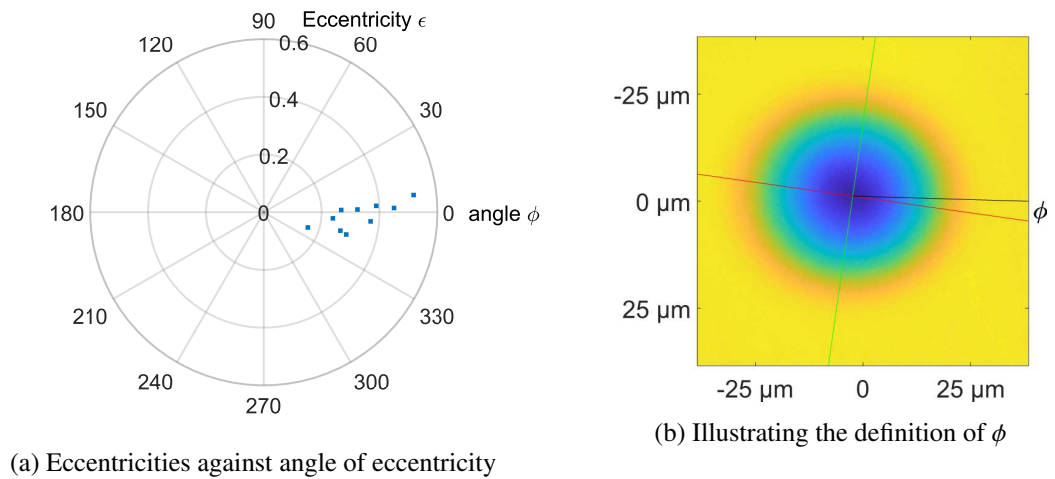


Figure 5.2: Plotting the eccentricities of the mirror structures against the orientation of the major axis of the 2D fit shows that there is still a preferred direction for the ellipticity

In their investigation of the influence of ablation laser polarization on the eccentricity of the created structure, Uphoff et.al. reported a mean eccentricity of 0.47 for a linearly polarized beam, with a preferred axis along the beam polarization, and a mean eccentricity of 0.26 for circular polarization, without a preferred axis [27]. In our case, we observe a mean eccentricity of 0.32 with a preferred axis. This means, numerically we are already on the better side of their spectrum, which is a very encouraging result. The remaining directional preference indicates, that there is still room for improvement. One of the causes might be the astigmatism discussed in section 3.1.2.

Summary and Outlook

6.1 Summary

For my master thesis project I have set up, characterized, and tested a new fiber mirror production setup.

All technical elements have been interfaced with the lab computer and can be controlled with the same self-written program. All aspects influencing the ablation parameters and their control have been characterized to enable a predictable ablation sequence, and to identify aspects that require additional optimization.

Furthermore, I have set up an interference microscope to profile the produced ablation crater. In the process, I have implemented, tested, and compared several analysis methods. These routines have been integrated into the control software to enable feedback.

Finally, I have tested the setup on a fused silica substrate and on fiber end facets. From these tests it could be concluded that the setup is working as expected. Additionally, further information on its characteristics and necessary future steps could be gathered.

6.2 Technical Improvements

While the new fiber mirror production facility has been successfully set up, there are a number of aspects which require further attention:

We need to attenuate the electronic noise created by the laser power supply (see section 3.1.1). For this purpose, a line filter could be attached directly to the housing of the power supply. If this does not reduce the noise significantly, a possible influence of the cables running from the power supply to the laser needs to be investigated.

Additional efforts should be made to find and - if possible - remove the source of the astigmatism of the focused beam (see section 3.1.3). If this is not achievable, steps need to be taken to correct for the astigmatism. Once we have a more symmetric beam, the eccentricity measurements can be repeated. On the basis of their results we can determine if it would be worthwhile to attempt to improve the circularity of the polarization even further.

In order for the setup to function as a facility to produce a large number of fiber mirrors, the time needed for each individual fiber should be as short as possible. The main bottleneck at the moment is the positioning procedure, especially the time needed to locate the fiber end facet in the interferometer field of view (see section 3.2.2). To accelerate this process, two steps can be taken. First, it should be attempted

to increase the contrast of the interferometer and remove the inhomogeneities in the illumination. This should allow for more robust computer routines to center the fiber automatically. Furthermore it would have the advantage of producing cleaner, easier to analyze interferograms, saving additional time during the surface profiling process. While first efforts to work with a diffuser have not been successful, the flexibility of the illumination setup leaves additional possibilities to be explored in that regard. The second approach is to couple light into the fiber, so that the position of the fiber core should appear as a bright spot, even if the end facet itself is not in the focal plane of the interferometer objective. This second step is also necessary to improve the precision of the fiber positioning. By taking an image of the illuminated fiber core and fitting a Gaussian to the intensity profile, one can determine the location of the fiber center to sub-pixel accuracy.

To remove the pulse power instabilities caused by the long rise time of the shutter (see section 3.2.3), it has already been decided to replace the shutter by an acousto-optic modulator (AOM). In this case we can keep the laser running constantly at a stable power, while pulses are then generated by switching on the AOM's RF drive signal for a set time and power. The resulting diffracted beam is used as the ablation pulse.

6.3 Advanced Techniques

The length of fiber cavities is mainly limited by two effects: Clipping losses and mode matching efficiency. Both these limitations can be overcome by applying further techniques.

6.3.1 Dot-Milling Technique

The current single pulse technique imprints the Gaussian shape of the laser beam intensity profile onto the fiber end facet. The resulting structure can only be approximated as spherical in a limited region around the center. As the diameter of the cavity mode at the mirror position increases with longer cavities, a larger part of the effective mirror profile becomes non-spherical, resulting in higher clipping losses and a decrease in the finesse. To produce larger mirrors with spherical curvature, a technique with multiple pulses, so-called dot-milling, can be used. Here, the ablation is performed with a whole sequence of weak pulses directed at different positions on the fiber end facet according to a pre-calculated pattern. Combining this method with the use of so-called "endlessly single-mode" photonic-crystal (PC) fibers [44], cavities with a length in the millimeter regime have been realized [17]. PC fibers have a larger mode field diameter than regular single mode fibers, which increases the mode matching efficiency in the case of a larger cavity mode spot size. The new translation stages have the high precision needed to implement the dot milling scheme in our setup.

6.3.2 GRIN Lenses

A different approach to address the decreased mode matching efficiency caused by the increased spot size is using a combination of single mode, graded index (GRIN) and multi-mode fibers [16]. Here, a GRIN fiber is spliced to the single mode fiber to act as a focusing element. It shapes the fiber mode to match the cavity mode in analogy to a focusing lens in the case of a free space cavity (see figure 6.1). A piece of multi mode fiber is spliced to this assembly as the mirror carrier and as a spacer to ensure the GRIN lens is positioned at the correct distance from the cavity. For this purpose, a new splicer¹ has already been bought.

¹Fujikura Fusion Splicer FSM 100P+

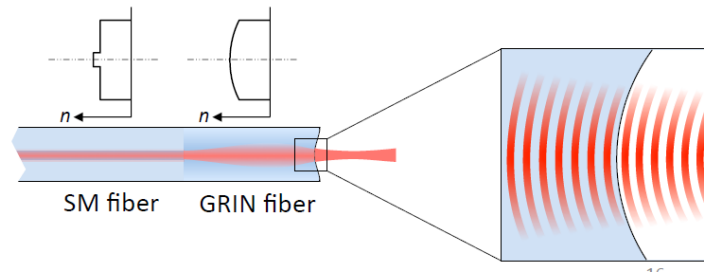


Figure 6.1: The graded refractive index shapes the fiber mode such that it matches the cavity mode at the mirror. (Simplified sketch, neglecting the multi-mode fiber spacer to illustrate the principle.)

With all these further improvements we expect that the new setup will be able to produce state of the art fiber mirrors in the future.

Bibliography

- [1] E. M. Purcell, “Spontaneous emission probabilities at radio frequencies”, *Physical Review*, vol. 69, 11-12, American Physical Society, 1946 681+,
URL: http://prola.aps.org/pdf/PR/v69/i11-12/p674%7B%5C_%7D2 (cit. on p. 1).
- [2] S. Haroche and D. Kleppner, *Cavity quantum electrodynamics*, *Physics Today* **42** (1989) 24 (cit. on p. 1).
- [3] P. Zoller et al., *Quantum information processing and communication*, *The European Physical Journal D - Atomic, Molecular, Optical and Plasma Physics* **36** (2005) 203, ISSN: 1434-6079, URL: <http://dx.doi.org/10.1140/epjd/e2005-00251-1> (cit. on p. 1).
- [4] S. Haroche and J. M. Raimond, *Exploring the Quantum: Atoms, Cavities, and Photons*, Oxford Graduate Texts, OUP Oxford, 2006, ISBN: 9780198509141,
URL: <https://books.google.de/books?id=ynwSDAAAQBAJ> (cit. on p. 1).
- [5] H. Mabuchi and A. C. Doherty, *Cavity Quantum Electrodynamics: Coherence in Context*, *Science* **298** (2002) 1372, ISSN: 0036-8075,
URL: <http://science.sciencemag.org/content/298/5597/1372> (cit. on p. 1).
- [6] A. D. Boozer et al., *Reversible State Transfer between Light and a Single Trapped Atom*, *Physical Review Letters* **98** (2007) 193601, ISSN: 0031-9007,
URL: <https://link.aps.org/doi/10.1103/PhysRevLett.98.193601> (cit. on p. 1).
- [7] R. Long et al., *Magnetic microchip traps and single-atom detection*, *Philosophical Transactions of the Royal Society of London A: Mathematical, Physical and Engineering Sciences* **361** (2003) 1375, ISSN: 1364-503X,
URL: <http://rsta.royalsocietypublishing.org/content/361/1808/1375>
(cit. on p. 1).
- [8] M. Trupke et al., *Microfabricated high-finesse optical cavity with open access and small volume*, *Applied Physics Letters* **87** (2005) 211106, URL: <http://dx.doi.org/10.1063/1.2132066> (cit. on p. 1).
- [9] T. Steinmetz et al., *Stable fiber-based Fabry-Perot cavity*, *Applied Physics Letters* **89** (2006) 111110, URL: <http://dx.doi.org/10.1063/1.2347892> (cit. on p. 1).
- [10] D. Hunger et al., *A fiber Fabry-Perot cavity with high finesse*, *New Journal of Physics* **12** (2010) 65038,
URL: <http://stacks.iop.org/1367-2630/12/i=6/a=065038> (cit. on pp. 1, 9, 13).
- [11] U. C. Paek and A. L. Weaver, *Formation of a Spherical Lens at Optical Fiber Ends with a CO₂ Laser*, *Appl. Opt.* **14** (1975) 294,
URL: <http://ao.osa.org/abstract.cfm?URI=ao-14-2-294> (cit. on p. 1).

- [12] F. Laguarda, N. Lupon and J. Armengol, *Optical glass polishing by controlled laser surface-heat treatment*, Appl. Opt. **33** (1994) 6508, URL: <http://ao.osa.org/abstract.cfm?URI=ao-33-27-6508> (cit. on p. 1).
- [13] M. Feit and A. Rubenchik, “Mechanisms of CO₂ laser mitigation of laser damage growth in fused silica”, vol. 4932, Proc. SPIE, 2003 91 (cit. on pp. 1, 10, 11).
- [14] D. Hunger et al., *Laser micro-fabrication of concave, low-roughness features in silica*, AIP Advances **2** (2012) 12119, URL: <http://dx.doi.org/10.1063/1.3679721> (cit. on pp. 1, 11, 35, 39).
- [15] D. Najer et al., *Fabrication of mirror templates in silica with micron-sized radii of curvature*, Applied Physics Letters **110** (2017) 11101, URL: <http://dx.doi.org/10.1063/1.4973458> (cit. on pp. 1, 2, 5, 7, 11).
- [16] G. Gulati et al., *Fiber cavities with integrated mode matching optics*, 2017, arXiv: arXiv:1703.03785 (cit. on pp. 2, 42).
- [17] K. Ott et al., *Millimeter-long fiber Fabry-Perot cavities*, Opt. Express **24** (2016) 9839, URL: <http://www.opticsexpress.org/abstract.cfm?URI=oe-24-9-9839> (cit. on pp. 2, 42).
- [18] J. Gallego et al., *High-finesse fiber Fabry-Perot cavities: stabilization and mode matching analysis*, Applied Physics B **122** (2016) 47, ISSN: 1432-0649, URL: <http://dx.doi.org/10.1007/s00340-015-6281-z> (cit. on pp. 2, 36).
- [19] T. G. Ballance et al., *Cavity-induced backaction in Purcell-enhanced photon emission of a single ion in an ultraviolet fiber cavity*, Physical Review A **95** (2017) 033812, ISSN: 2469-9926, URL: <https://link.aps.org/doi/10.1103/PhysRevA.95.033812> (cit. on p. 2).
- [20] H. Takahashi et al., *Cavity-induced anti-correlated photon emission rates of a single ion*, (2017), arXiv: 1705.07923, URL: <http://arxiv.org/abs/1705.07923> <http://dx.doi.org/10.1103/PhysRevA.96.023824> (cit. on p. 2).
- [21] A. Muller et al., *Coupling an epitaxial quantum dot to a fiber-based external-mirror microcavity*, Applied Physics Letters **95** (2009) 173101, ISSN: 0003-6951, URL: <http://aip.scitation.org/doi/10.1063/1.3245311> (cit. on p. 2).
- [22] S. Bogdanović et al., *Design and low-temperature characterization of a tunable microcavity for diamond-based quantum networks*, Applied Physics Letters **110** (2017) 171103, ISSN: 0003-6951, URL: <http://aip.scitation.org/doi/10.1063/1.4982168> (cit. on p. 2).
- [23] N. E. Flowers-Jacobs et al., *Fiber-cavity-based optomechanical device*, Applied Physics Letters **101** (2012) 221109, ISSN: 0003-6951, URL: <http://aip.scitation.org/doi/10.1063/1.4768779> (cit. on p. 2).
- [24] C. Miller and F. Janniello, *Passively temperature-compensated fibre Fabry-Perot filter and its application in wavelength division multiple access computer network*, Electronics Letters **26** (1990) 2122, ISSN: 00135194, URL: http://digital-library.theiet.org/content/journals/10.1049/el%7B%5C_%7D19901365 (cit. on p. 2).

- [25] M. Mader et al., *A scanning cavity microscope*, Nature Communications **6** (2015) 7249, ISSN: 2041-1723, URL: <http://www.nature.com/doi/finder/10.1038/ncomms8249> (cit. on p. 2).
- [26] R. Kitamura, L. Pilon and M. Jonasz, *Optical constants of silica glass from extreme ultraviolet to far infrared at near room temperature*, Appl. Opt. **46** (2007) 8118, URL: <http://ao.osa.org/abstract.cfm?URI=ao-46-33-8118> (cit. on pp. 2, 9, 10).
- [27] M. Uphoff et al., *Frequency splitting of polarization eigenmodes in microscopic Fabry-Perot cavities*, New Journal of Physics **17** (2015) 13053, URL: <http://stacks.iop.org/1367-2630/17/i=1/a=013053> (cit. on pp. 2, 6, 17, 39, 40).
- [28] B. E. A. Saleh and M. C. Teich, *Fundamentals of photonics*, Wiley-Interscience, 2007 1177, ISBN: 0471358320 (cit. on pp. 4, 9).
- [29] R. Reimann, *Cooling and Cooperative Coupling of Single Atoms in an Optical Cavity*, PhD thesis: Rheinische Friedrich-Wilhelms-Universität Bonn, 2014 (cit. on p. 7).
- [30] J. Gallego, *Strong Coupling between Small Atomic Ensembles and an Open Fiber Cavity*, PhD thesis: Rheinische Friedrich-Wilhelms-Universität Bonn, 2017 (cit. on pp. 7, 21).
- [31] G. A. J. Markillie et al., *Effect of vaporization and melt ejection on laser machining of silica glass micro-optical components*, Appl. Opt. **41** (2002) 5660, URL: <http://ao.osa.org/abstract.cfm?URI=ao-41-27-5660> (cit. on p. 9).
- [32] D. Hunger, *Herstellung und Charakterisierung von Faserresonatoren hoher Finesse*, Diplomarbeit: Ludwig-Maximilians-Universität München, 2005 (cit. on pp. 10, 11, 35).
- [33] C. Deutsch, *High finesse fibre Fabry-Perot resonators Production, characterization and applications*, Diplomarbeit: Ludwig-Maximilians Universität München, 2008 (cit. on p. 10).
- [34] A. D. McLachlan and F. P. Meyer, *Temperature dependence of the extinction coefficient of fused silica for CO₂ laser wavelengths*, Applied Optics **26** (1987) 1728, ISSN: 0003-6935, URL: <https://www.osapublishing.org/abstract.cfm?URI=ao-26-9-1728> (cit. on p. 11).
- [35] D. Meschede, *Optics, Light and Lasers*, Wiley-VCH Verlag GmbH & Co. KGaA, 2006, ISBN: 9783527618873, URL: <http://doi.wiley.com/10.1002/9783527618873> (cit. on p. 14).
- [36] F. K. Kneubühl and M. W. Sigrist, *Laser*, Vieweg+Teubner Verlag, 1989, ISBN: 978-3-519-33032-5, URL: <http://link.springer.com/10.1007/978-3-663-01450-8> (cit. on pp. 14, 15).
- [37] Synrad, *Polarization effects in metals, ceramics and acrylic (white paper)* (cit. on p. 17).
- [38] F. Keilmann and Y. H. Bai, *Periodic surface structures frozen into CO₂ laser-melted quartz*, Applied Physics A Solids and Surfaces **29** (1982) 9, ISSN: 0721-7250, URL: <http://link.springer.com/10.1007/BF00618110> (cit. on p. 17).

- [39] L. Mingzhou, *Development of fringe analysis techniques in white light interferometry for micro-component measurement*, PhD thesis: National University of Singapore, 2008, URL: http://scholarbank.nus.edu.sg/bitstream/handle/10635/15866/Thesis%7B%5C_%7DPhD%7B%5C_%7DHT030760Y.pdf?sequence=1 (cit. on p. 27).
- [40] A. H. Mirau, "Interferometer", U.S. patent 2,612,074, 1952, URL: <https://www.google.com/patents/US2612074> (cit. on p. 29).
- [41] B. Bowe, *White light interferometric surface profiler*, Optical Engineering **37** (1998) 1796, ISSN: 0091-3286, URL: <http://opticalengineering.spiedigitallibrary.org/article.aspx?doi=10.1117/1.601727> (cit. on p. 31).
- [42] G. S. Kino and S. S. C. Chim, *Mirau correlation microscope*, Appl. Opt. **29** (1990) 3775, URL: <http://ao.osa.org/abstract.cfm?URI=ao-29-26-3775> (cit. on p. 33).
- [43] T. Mario Costantini, *A novel phase unwrapping method based on network programming*, IEEE Transactions on Geoscience and Remote Sensing **36** (1998) 813, ISSN: 01962892 (cit. on p. 34).
- [44] T. A. Birks, J. C. Knight and P. S. J. Russell, *Endlessly single-mode photonic crystal fiber*, Optics Letters **22** (1997) 961, ISSN: 0146-9592, URL: <https://www.osapublishing.org/abstract.cfm?URI=ol-22-13-961> (cit. on p. 42).

Appendix

Knife Edge Method

The knife edge method is a technique to profile a beam with a Gaussian transversal intensity profile

$$I(x, y) = I_0 \exp\left(\frac{-2x^2}{w_x^2}\right) \exp\left(\frac{-2y^2}{w_y^2}\right), \quad (\text{A.1})$$

with w_x and w_y being the beam radii in x- and y-direction respectively, and the beam travelling in the z-direction. The total power is then given by the integral

$$P_{\text{tot}} = I_0 \int_{-\infty}^{\infty} \exp\left(\frac{-2x^2}{w_x^2}\right) dx \int_{-\infty}^{\infty} \exp\left(\frac{-2y^2}{w_y^2}\right) dy = \frac{\pi}{2} I_0 w_x w_y \quad (\text{A.2})$$

If the beam is now partially blocked by a knife edge (see figure A.1 (a)), in our case a standard razor blade, coming in from the positive x-direction, the remaining transmitted power as a function of knife edge position X is

$$P(X) = I_0 \int_{-\infty}^X \exp\left(\frac{-2x^2}{w_x^2}\right) dx \int_{-\infty}^{\infty} \exp\left(\frac{-2y^2}{w_y^2}\right) dy = \frac{P_{\text{tot}}}{2} \left[1 - \text{erf}\left(\frac{\sqrt{2}X}{w_x}\right) \right] \quad (\text{A.3})$$

The beam radius w_x can now be determined by moving the razor blade step wise through the beam from fully covered to fully open, recording the transmitted power as a function of position, and fitting a function based on the right hand side of equation A.3 to the data. Examples can be seen in figure A.2. By repeating the procedure for different z-positions (see figure A.1 (b)), the beam waist can be determined.

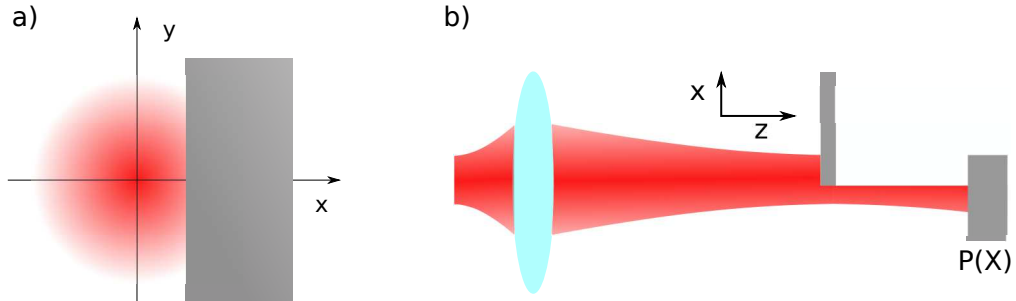
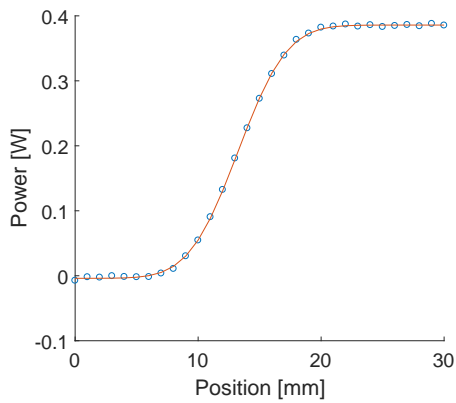
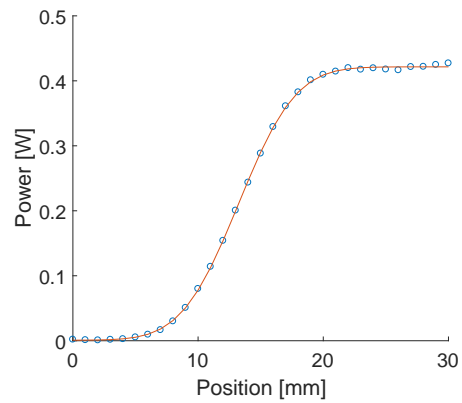


Figure A.1: Knife edge method to determine the profile of a Gaussian beam: Measuring the transmitted power for different x -position reveals the transversal profile (a), repeating the measurement for different z -positions allows to determine the axial profile as well. (b)



(a) Expanded beam of the telescope with a beam diameter of 12.5 ± 0.5 mm. The dip at the end is attributed to fluctuations of the laser at low powers.



(b) Beam right before the focusing lens. It has further expanded to $d = 14 \pm 0.5$ mm.

Figure A.2: Knife edge method curves for the expanded beam.

List of Figures

2.1	Field in Fabry-Perot resonators	4
2.2	Intensity for different finesses	4
2.3	Mode matched cavity	5
2.4	Stability diagram for Fabry-Perot resonators	6
2.5	Gaussian Beam	7
2.6	Cavity type comparision	7
2.7	Mode mismatch between fiber and cavity	8
2.8	Single mode fiber	9
2.9	Different fiber types	9
2.10	Wavelength dependence of the ablation process	10
3.1	Steps of fiber cavity construction	13
3.2	Laser levels	14
3.3	CO ₂ laser in wave guide configuration	14
3.4	Laser power stability	15
3.5	Power fluctuation analysis	16
3.6	Power meter noise analysis	16
3.7	Optical Setup	17
3.8	Phase shifting mirror	18
3.9	Circular polarization measurement	19
3.10	Long range beam profile	19
3.11	Beam profile near waist	20
3.12	Mirror decentration	21
3.13	Cleaved end facet comparison	21
3.14	Fiber end facet in interferometer focus	22
3.15	Ablation sequence	23
3.16	Shutter characterization	23
3.17	Pulse shapes for different pulse durations	24
3.18	Grahical user interface	26
4.1	Mirau interferometer	28
4.2	Mirau Objective	29
4.3	Interferometry Frames	29
4.4	PIFOC Stability	30
4.5	Machined fiber tip	31
4.6	Interferograms for the brightest pixel method	32
4.7	Surface with brightest pixel method	32
4.8	Principle of Fourier analysis	33

List of Figures

4.9	Surface with Fourier analysis method	34
4.10	Fitted fringes	35
4.11	Surface with phase unwrapping method	35
4.12	2D Gaussian fit	36
4.13	Fits to cross section centers	36
4.14	Direct method comparison	38
5.1	Structure depth vs radius of curvature	40
5.2	Eccentricities of ablation craters	40
6.1	Mode matching with GRIN lens	43
A.1	Knife edge method	52
A.2	Expanded beam size	52

Acknowledgements

First of all, I would like to thank Prof. Meschede for giving me the opportunity to work on this interesting project in his group.

Then, I would like to thank Wolfgang Alt for planning the whole project and for his support throughout my work.

I would also like to thank the whole FCQED team, especially Miguel Martinez-Dorantes for getting me started, Jose Gallego for sharing his experience with the old setup with me, Deepak Pandey for all his support, and everyone in the group for the helpful discussions.

On the technical side, I would like to thank Mr Langen and the mechanical workshop for designing and manufacturing the bulb holder for the interferometer, and Mr Brähler and the electronics workshop for their support regarding the various laser connections.

Finally, I would like to thank Prof. Linden for agreeing to be my second referee.